Myotubularin-related-protein-7 inhibits mutant (G12V) K-RAS by direct interaction

Journal Article

Author(s):
Weidner, Philip; Saar, Daniel; Söhn, Michaela; Schroeder, Torsten; Yu, Yanxiong; Zöllner, Frank G.; Ponelies, Norbert; Zhou, Xiaobo; Zwicky, André; Rohrbacher, Florian N.; Pattabiraman, Vijaya R.; Tanriver, Matthias; Bauer, Alexander; Ahmed, Hazem (ID); Ametamey, Simon M.; Riffel, Philipp; Seger, Rony; Bode, Jeffrey W.; Wade, Rebecca C.; Ebert, Matthias P.A.; Kragelund, Birthe B.; Burgermeister, Elke

Original Articles

Myotubularin-related-protein-7 inhibits mutant (G12V) K-RAS by direct interaction

Philip Weidner [a], Daniel Saar [b], Michaela Söhn [a], Torsten Schroeder [a], Yanxiong Yu [a], Frank G. Zöllner [c,d,e], Norbert Ponelies [f], Xiaobo Zhou [g], André Zwicky [h], Florian N. Rohrbacher [h], Vijaya R. Pattabiraman [h], Matthias Tanriver [h], Alexander Bauer [b], Hazem Ahmed [i], Simon M. Ametamey [i], Philipp Riffel [j], Rony Seger [k], Jeffrey W. Bode [h], Rebecca C. Wade [l,m], Matthias P.A. Ebert [a,n], Birthe B. Kragelund [b,1,**], Elke Burgermeister [a,1,*]

[a] Department of Medicine II, Medical Faculty Mannheim, Heidelberg University, Mannheim, Germany
[b] Structural Biology and NMR Laboratory (SBiNLab) and the Linderstrøm-Lang Centre for Protein Science, Department of Biology, University of Copenhagen, Copenhagen, Denmark
[c] Computer Assisted Clinical Medicine, Medical Faculty Mannheim, Heidelberg University, Mannheim, Germany
[d] Mannheim Institute for Intelligent Systems in Medicine, Medical Faculty Mannheim, Heidelberg University, Mannheim, Germany
[e] Cooperative Core Facility Animal Scanner ZI, Medical Faculty Mannheim, Heidelberg University, Mannheim, Germany
[f] Orthopaedics & Trauma Surgery, Medical Faculty Mannheim, Heidelberg University, Mannheim, Germany
[g] Department of Medicine I, Medical Faculty Mannheim, Heidelberg University, Mannheim, Germany
[h] Laboratory of Organic Chemistry, Department of Chemistry and Applied Bioscience of ETH, Zurich, Switzerland
[i] Institute of Pharmaceutical Sciences, Department of Chemistry and Applied Biosciences of ETH, Zurich, Switzerland
[j] Clinic of Radiology and Nuclear Medicine, Medical Faculty Mannheim, Heidelberg University, Mannheim, Germany
[k] Department of Immunology and Regenerative Biology, Weizmann Institute of Science, Rehovot, Israel
[l] Heidelberg Institute for Theoretical Studies (HITS), Heidelberg, Germany
[m] Heidelberg University, Zentrum für Molekulare Biologie (ZMBH), DKFZ-ZMBH Alliance, and Interdisciplinary Center for Scientific Computing (IWR), Heidelberg, Germany
[n] DKFZ-Hector Institute at the University Medical Center, Mannheim, Germany

ARTICLE INFO

ABSTRACT

Inhibition of K-RAS effectors like B-RAF or MEK1/2 is accompanied by treatment resistance in cancer patients via re-activation of PI3K and Wnt signaling. We hypothesized that myotubularin-related-protein-7 (MTMR7), which inhibits PI3K and ERK1/2 signaling downstream of RAS, directly targets RAS and thereby prevents resistance. Using cell and structural biology combined with animal studies, we show that MTMR7 binds and inhibits RAS at cellular membranes. Overexpression of MTMR7 reduced RAS GTPase activities and protein levels, ERK1/2 phosphorylation, c-FOS transcription and cancer cell proliferation in vitro. We located the RAS-inhibitory activity of MTMR7 to its charged coiled coil (CC) region and demonstrate direct interaction with the gastrointestinal cancer-relevant K-RAS^{G12V} mutant, favouring its GDP-bound state. In mouse models of gastric and intestinal cancer, a cell-permeable MTMR7-CC mimicry peptide decreased tumour growth, Ki67 proliferation index and ERK1/2 nuclear positivity. Thus, MTMR7 mimicry peptide(s) could provide a novel strategy for targeting mutant K-RAS in cancers.

Abbreviations

aa	amino acid
Ab	antibody
AKT	protein kinase B
APC	adenomatous polyposis coli
CC	coiled coil
CD	circular dichroism
CEA	carcinoembryonic antigen
CRC	colorectal cancer
EGF(R)	epidermal growth factor (receptor)
ERK1/2	extracellular signal-regulated kinase-1/2
EV	empty vector
FCS	fetal calf serum
FFPE	formalin-fixed-paraffin-embedded
FI	fluorescence intensity
FL	full-length
FOS	FBJ murine osteosarcoma viral oncogene homologue
GAP	GTPase activating protein
GD	globular domain
GDS	guanine nucleotide dissociation factor
GEF	guanine nucleotide exchange factor
GFP	green fluorescence protein
GI	gastrointestinal
H&E	haematoxylin&eosin
HSP90	heat shock protein 90
HCS	catalytical site (MTMs)
HVR	hypervariable region
IB	immunoblotting
IF	immunofluorescence
IHC	immunohistochemistry
Ins(1,3)P$_2$	inositol-1,3-bisphosphate
KCA3.1	calcium-activated potassium channel SK4
K-RAS	Kirsten rat sarcoma viral oncogene homologue
M7-CC514-554	recombinant MTMR7-CC mimicry protein
MD	molecular dynamics
MEK1/2	mitogen-activated kinase kinase-1/2
MT	synthetic MTMR7-CC mimicry peptide
MTM	myotubularin
MTMR7	myotubularin-related-protein-7
MRI	magnetic resonance imaging
mTOR	mechanistic target of rapamycin kinase
NMR	nuclear magnetic resonance
OD	optical density
PET/CT	positron emission tomography/computed tomography
PH	plextrin homology (domain)
PI	phosphatidyl-inositol
PI3K	phosphoinositide-3-kinase
PI(3)P	phosphatidyl-inositol-3-monophosphate
PI(3,5)P$_2$	phosphatidyl-inositol-3,5-bisphosphate
PIP	phosphoinositide
PLC	phospholipase C
PS	phosphatidylserine
PTP	protein tyrosine phosphatase
RAF	proto-oncogene serine/threonine-protein kinase
RAB	Ras-related protein
RAL	Ras-like proto-oncogene
S6RP	S6 ribosomal protein
SC	scrambled control peptide
SCF	subcellular fractionation
SID	SET-interaction domain
SOS	Son of Sevenless Homologue
SRE	serum-response element
SV40	simian virus-40
t	time
TAg	large T-antigen
UT	untreated (control)
VC	vehicle control
WT	wild-type

1. Introduction

Activating mutations in rat sarcoma viral oncogene homologue (*RAS*) genes downstream of the epidermal growth factor receptor (EGFR) family [1] are frequent in gastrointestinal (GI) cancers, including tumours of the pancreas, colorectum and stomach. Therein, the three *RAS* genes, *K-RAS, N-RAS* and *H-RAS* drive both cancer initiation and progression. Constitutive stimulation of the EGFR-RAS-mitogen-activated-protein-kinase-kinase (MEK)1/2-extracellular-regulated-protein-kinase (ERK)1/2 cascade [2] is a major obstacle for effective treatment in advanced disease [3], and new druggable targets, which inhibit mitogenic RAS signaling, are of medical need [4,5]. Current clinically used K-RAS inhibitors are mutation-specific, such as covalent inhibitors (e.g. Sotorasib) of the G12C K-RAS variant common in lung cancer [6]. This approach does not cover most GI cancer-relevant mutations, including the G12D, G12V and G13D K-RAS proteins. Inhibition of RAS regulators or effectors has also been proposed, e.g. by interference with binding of son-of-sevenless (SOS), a guanine nucleotide exchange factor (GEF) that acts on RAS [7,8]. However, these developments have so far not reached the clinic.

In addition to regulation by GEFs and GTPase activating proteins (GAPs), the activity and stability of K-RAS depend on its interaction with the plasma membrane and cellular endomembranes via hydrophobic and electrostatic contacts [9]. Specifically, the globular catalytic GTP-binding domain (GD) and the hypervariable region (HVR) of the GI cancer-relevant K-RAS4B isoform account for the signal output generated by the GTPase. The C-terminal HVR is a polybasic, lysine-rich "tail"

which carries a post-translational modification motif (CAAX) that allows farnesylation and membrane insertion of the protein.

Negatively charged phosphatidyl-serine (PS) and phosphatidyl-inositides (PIPs) at the inner leaflet of the phospholipid bilayer bind RAS proteins, a mechanism crucial for the activation of downstream signaling [10]. Alterations in the electrostatic potential across the membrane, either by voltage-gated ion channels or enzymes (e.g. sphingomyelinase) result in rapid re-localization of RAS proteins [11] and trafficking to subcellular compartments, leading either to their degradation or recycling via vesicles of endosomes, lysosomes and the endoplasmic reticulum/trans-Golgi network [10]. However, the molecular mechanism by which K-RAS is re-localized and how it is subsequently deactivated remains undefined, leaving a knowledge gap in the understanding of how K-RAS and its activated variants can be specifically targeted towards inactivation.

We recently described myotubularin-related-protein-7 (MTMR7) [12], a member of the myotubularin (MTM) family of PIP phosphatases [13], as a dual inhibitor of ERK1/2 and phosphoinositide-3-kinase (PI3K) signaling and as an activator of the transcription factor peroxisome-proliferator-activated-receptor-gamma (PPARγ) [14,15], which promotes cell differentiation, host immunity and metabolism. From N-to-C-terminal, MTMs consist of plextrin homology (PH), protein tyrosine phosphatase (PTP), SET-interaction (SID) and coiled coil (CC) domains [16]. Catalytically active members form heterodimers with enzymatically inactive enzymes, e.g., MTMR6/7/8 with MTMR9 [17]. Overall, MTMs are membrane-bound and dephosphorylate phosphatidyl-inositol-3-monophosphate (PI(3)P) and −3,

5-bisphosphate (PI(3,5)P2) at the 3′-position [18]. In addition to the localization of MTMs at cellular membranes, MTMR7 also resides in a soluble form in the cytoplasm [12], where it metabolizes free inositol-1, 3-bisphosphate (Ins(1,3)P2). Hitherto, the specific role of MTMR7 in tumour cells remains elusive.

We previously showed that MTMR7 expression is frequently lost in tumour tissues from patients with colorectal cancer (CRC) [15]. We mapped the active region of MTMR7 responsible for PPARγ binding and activation to its CC domain [14]. Supplementation of a cell membrane-permeable MTMR7 mimicry peptide corresponding to this CC domain (MTMR7-CC) recapitulated the effects of pharmacological PPARγ activation *in vitro* and *in vivo* [14], and is thus expected to restore the tumour suppressor functions of MTMR7 [14].

Based on the functions of MTMs in endocytosis, subcellular traffic and recycling of the EGFR at intracellular membranes (e.g. endosomes) [19] together with the potent inhibition of ERK1/2 by MTMR7 [15], we hypothesized that the effect exerted by MTMR7 could be based on a direct inhibition of EGFR-activated RAS at cellular membranes, followed by mitigation of downstream signaling and tumour cell proliferation. Using a combination of cell and structural biology, and exploring mouse models, we demonstrate that MTMR7 co-localizes and directly interacts with the GI cancer-relevant K-RAS^{G12V} mutant by means of its CC domain. Overexpression of MTMR7 decreased the activity of RAS proteins and reduced proliferation of human *KRAS*-mutated GI cancer cells *in vitro* and attenuated murine tumour growth *in vivo*. These efficacies were phenocopied by the previously designed MTMR7-CC peptide [14, 15]. Our results offer detailed insight into a novel regulatory mechanism of K-RAS4B, which could be explorable for drug discovery and inhibition of mutant *KRAS* in human GI cancers.

2. Materials and Methods

2.1. Reagents

Chemicals were purchased from Merck (Darmstadt, Germany) or Sigma (Heidelberg, Germany). Antibodies (Abs) and their applications are listed in Table S1.

2.2. DNA-constructs

Human full-length (FL) MTMR7 cDNA (start codon MEHIRT, aa 1-660, 76 kDa, NM_004686.4) was in pTarget (pT) vector (Promega GmbH, Mannheim, Germany) with or without green fluorescent protein (GFP) or FLAG tag [15]. Transient transfection and luciferase assays were performed as described [20].

2.3. Design and synthesis of peptides

The MTMR7-CC (MT) peptide corresponded to the C-terminal leucine-rich amino acid (aa) sequence of human MTMR7 full-length (FL) protein (aa 521-550; SwissProt ID: Q9Y216.3: **L**MAVKEETQQ**LEEELEALEERL**EKIQKVQ**L**). The scrambled control (SC) peptide was designed based on the MT sequence using the random scrambling web tool (https://web.expasy.org/randseq/: VLQEEILE MTEEKALLQALLKKEQERVQEE). The peptides were synthesized by an automatic device with a myristic acid at the N-terminus and an amide at the C-terminus (ETH Zürich, Switzerland). Quality validation of sequence and purity was done by mass spectrometry, and the peptides were provided as lyophilized powder [21] as published previously [14, 15].

2.4. Cloning, expression and purification of recombinant proteins

The human MTMR7-CC cDNA (corresponding to aa residues R514 to K554, M7-CC) was cloned into a modified pET24a vector, encoding an N-terminal hexahistidine- and SUMO-tag (H$_6$-SUMO). For

quantification, a tryptophan at position 517 was added outside of the CC sequence to minimize potential effects on CC formation.

After transformation of *E. coli* BL21(-DE3) (New England BioLabs, Frankfurt, Germany) with the plasmid, the M7-CC protein was produced using high salt Lysogeny Broth (LB) Medium at 37 °C, and expression was induced at an OD$_{600}$ 0.8–1.2 with 0.5 mM isopropyl-β-D-thio-galactopyranoside (IPTG) for 4 h under shaking at 180 rpm. For isotope-labelled protein production, M9 minimal medium, containing ^{15}NH$_4$Cl as sole nitrogen source and ^{13}C-glucose as sole carbon source was employed. Cells were harvested by centrifugation at 5.000×g for 20 min and resuspended in lysis buffer (20 mM imidazole, 4 M urea, 50 mM Tris pH 8, 200 mM NaCl, 10 % (*v/v*) glycerol). All buffers contained 5 mM β-mercaptoethanol. Then, cells were lysed using a cell disrupter (Constant Systems Ltd., Daventry, UK) at 25 kpsi. The lysate was cleared by centrifugation at 20.000×g for 45 min, and the supernatant passed two times over 1 mL Ni-NTA resin (Qiagen, Hilden, Germany) which had been pre-equilibrated with lysis buffer. The resin was subsequently washed with 20 mL lysis buffer, 20 mL buffer B (10 mM imidazole, 50 mM Tris pH 8, 1 M NaCl, 10 % (*v/v*) glycerol), 20 mL buffer C (20 mM imidazole, 1 % Triton X-100, 50 mM Tris pH 8, 200 mM NaCl, 10 % (*v/v*) glycerol) and 20 mL lysis buffer without urea. The M7-CC protein was then retrieved with elution buffer (500 mM imidazole, 50 mM Tris pH 8, 200 mM NaCl, 10 % (*v/v*) glycerol) and dialysed into lysis buffer without urea and imidazole, together with 0.1 mg His-tagged ULP1-protease, purified as described in Ref. [22]. After cleavage, the dialysed sample was passed again over 1 mL Ni-NTA resin to remove the uncleaved protein and the protease. The flow through was then concentrated to 1–2 mL, dialysed against 25 mM Tris pH 8 and purified on a HiTrap Q FF 5 mL column using an ÄKTA pure 25 chromatography system (GE Healthcare, Munich, Germany). A gradient from 20 to 50 % (*v/v*) of elution buffer (25 mM Tris pH 8, 1 M NaCl) over 25 column volumes was used. The fractions containing pure M7-CC protein were pooled, the buffer changed into 25 mM ammonium-bicarbonate pH 9, and aliquots were flash-frozen with liquid N$_2$ and freeze-dried.

K-RAS wildtype (WT) and K-RAS G12V mutant full-length (FL) proteins and the corresponding variants lacking the HVR (ΔHVR, corresponding to residues 1-169) were cloned into the same vector as above with an N-terminal His$_6$-SUMO-tag and produced in BL21 cells with auto-induction medium [23] at 37 °C. Expression was started at an OD$_{600}$ of 0.6 by changing the temperature from 37 °C to 18 °C and allowed to proceed for 24 h. Cells where then harvested, and the lysate was collected as mentioned above (lysis buffer: 20 mM imidazole, 40 mM HEPES pH 8, 500 mM NaCl, 5 mM MgCl$_2$, 10 % (*v/v*) glycerol). All buffers were supplemented with 5 mM β-mercaptoethanol. The supernatant was passed over a Ni-NTA resin as described before. Wash steps were done first with lysis buffer, followed by a wash step with lysis buffer supplemented with 1 M NaCl, and finally with lysis buffer again. Thereafter, the bound proteins were retrieved with elution buffer (lysis buffer supplemented with 500 mM imidazole). The protein was cleaved for 72 h at room temperature with ULP1-protease in a buffer containing 40 mM HEPES, pH 8, 0.01 % (*v/v*) Triton X-100, 10 % (*v/v*) glycerol, 5 mM MgCl$_2$, 200 mM NaCl and 10 mM β-mercaptoethanol. Uncleaved proteins and the His$_6$-SUMO tags were removed by passing the solution over the Ni-NTA column. The proteins were further purified by ion exchange chromatography using a HiTrap SP FF 5 mL column for FL proteins and a HiTrap QFF 5 mL column for ΔHVR proteins, by means of an ÄKTA pure 25 chromatography system (GE Healthcare, Munich, Germany) and size exclusion chromatography using a Superdex 200 Increase 10/300 GL. The ion exchange buffers contained 25 mM bis-Tris pH 7.4, 5 % (*v/v*) glycerol and 5 mM MgCl$_2$. The elution buffer contained the same components, but was additionally supplemented with 1 M NaCl. The size exclusion buffer contained 40 mM HEPES pH 8, 500 mM NaCl, 5 mM MgCl$_2$ and 5 % (*v/v*) glycerol. To control the nucleotide cargo, a nucleotide exchange was performed as described in Ref. [24]. Nucleotides were GDP and GTPγS purchased from Biolog Life Science Institute (Bremen, Germany).

The K-RAS HVR mimicking peptide (K-RAS4B$_{159-188}$) was produced at the ETH (Zürich, Switzerland) with 95 % purity and was further purified by HPLC.

2.5. Animals

The animal studies were conducted in agreement with the ethical guidelines of the University of Heidelberg and approved by the Government of Baden-Württemberg, Karlsruhe, Germany (G-188/18). C57BL/6J *CEA424-SV40* TAg mice were described before [25]. Female animals (2 months of age, average body weight 20 g) received food and water *ad libitum* before drug administration. The MTMR7-CC (MT) and scrambled control (SC) peptides were dissolved in sterile DMSO diluted in PBS and administered intraperitoneally (i.p.) as a single dose of 30 mg/kg per day, 4 times per week for 2 weeks. C57BL/6J *Apc^{min/+}* mice were purchased from Jackson Labs. (Bar Harbour, MA). Male animals (10 weeks of age, average body weight 23g) were treated as indicated above. Thereafter, the animals were sacrificed, and the organs snap-frozen in liquid N$_2$ or processed for formalin-fixation-and-paraffin-embedding (FFPE).

2.6. Magnetic resonance imaging (MRI)

MRI was performed on a 9.4T scanner (BioSpec 94/20 AVIII, Bruker BioSpin MRI GmbH, Ettlingen, Germany) using a transmit-receive volume resonator. After running T1-weighted fast low angle shot (FLASH) and T2-weighted spin echo rapid acquisition with relaxation enhancement (RARE) sequence in axial and coronal direction for localization of the stomach and the tumour, a high resolution 2D T2-weighted TurboRARE sequence with parameters echo time (TE)/repetition time (TR)/ flip angle (FA) = 20 ms/1364 ms/90°, echo train length = 8, averages = 22, field of view (FOV) = 30 mm^2, matrix = 192x192 resulting in an in-plane resolution of 0.156 mm^2. In total, 15 slices with a slice thickness of 0.25 mm were acquired.

In addition, a 2D diffusion weighted single shot spin echo sequence with parameters TE/TR/FA = 17 ms/1500 ms/90°, averages = 2, FOV = 30 mm^2, matrix = 128 x 128, resulting in an in-plane resolution of 0.25 mm^2 was recorded. In total, 15 slices with a slice thickness of 0.25 mm were acquired. Four diffusion values were selected (b = 0, 400, 800, 1400 s/mm^2). In both sequences, fat saturation was performed. This image acquisition was repeated after oral injection of 250 μl mannitol (2.5 % *w/v*) to fill the stomach and to alter the contrast between the stomach, the stomach wall and the tumour. The tumour volume was determined in axial, T2 weighted images after mannitol application using Horos (software version 3.14.006; https://horosproject.org).

2.7. Immunohistochemistry (IHC)

Haematoxylin & Eosin (HE) and antibody (Ab) staining were conducted on deparaffinized FFPE tissue sections as described [15]. For IHC, antigen retrieval was done with heating in citrate buffer, and H$_2$O$_2$ to block endogenous peroxidase activity. Staining was then processed using Abs (at a dilution of 1:100-1:250) followed by detection with 3, 3′-diaminobenzidine (DAB, VectorLabs, Peterborough, UK) and counterstaining with haematoxylin. 2D images of tumour or adenoma tissues were taken at a magnification of 100-200x. Qualitative and quantitative microscopic analysis (n = 5 fields per animal) was done manually and supported by Image J (imagej.nih.gov/ij). Tumour areas were measured in H&E stainings, then normalized to the area of the lamina muscularis mucosae and calculated in μm^2. The number of tumour cells with nuclear positivity of Ki67 was counted per field and normalized to the tumour area in μm^2 in the same field. The number of tumour cells with ERK1/2+ nuclei was counted per field and normalized either to the tumour area (*CEA-SV40* TAg) or to the total nuclei count (*Apc^{min/+}*) in the same field. The analyses were conducted observer-blinded using a standard bright-field microscope.

2.8. Cell culture and assays

Human embryonic kidney (HEK293T) and GI adenocarcinoma cell lines (all from the American Type Culture Collection (ATCC), Rockville, MD) were maintained as given by the provider. Colorimetric viability assays using 1-(4,5-dimethylthiazol-2-yl) 3,5-diphenyl-formazan (MTT) were conducted according to the manufacturer (Roche Diagnostics, Mannheim, Germany).

2.9. Subcellular fractionation, RAS pull-down, Western blot

Methods were performed as detailed elsewhere [26,27]. Briefly, total cell lysates were prepared from cells and subjected to immunoprecipitation (IP), followed by SDS-PAGE and detection by Western (immuno) blot (IB). Subcellular fractionation (SCF) followed a previous protocol [26,27]. RAS pull-down (GTPase activity) assays were conducted as recommended by the manufacturer (Biocat, Heidelberg, Germany).

2.10. Immunofluorescence (IF)

Staining and image acquisition was done as before [28,29]. Automatic counting of fluorescence signals (n ≥ 5 cells per field, n = 5 fields per image) from Abs and 4′,6′-diamidino-2-phenylindole (DAPI) was performed with Image J (imagej.nih.gov/ij). The actin cytoskeleton was visualized with phalloidin dye. Ab staining and image acquisition were conducted in triple colour mode as described and as given by the manufacturer (Zeiss GmbH, Hallbergmoos, Germany).

2.11. Patch-clamp

Standard patch-clamp recording techniques were used to measure currents in the whole-cell configuration. Patch electrodes were pulled from borosilicate glass capillaries (MTW 150F; World Precision Instruments, Friedberg Germany) using a DMZ-Universal Puller (Zeitz-Instrumente Vertriebs GmbH, Planegg, Germany). The electrodes were filled with pre-filtered pipette solution (126 mM KCl, 6 mM NaCl, 1.2 mM MgCl$_2$, 5 mM EGTA, 11 mM glucose, 1 mM MgATP, 0.1 mM Na$_3$GTP, and 10 mM HEPES adjusted to pH 7.2 with KOH).

Currents were recorded at room temperature with an EPC-8 amplifier (HEKA Elektronik, Stuttgart, Germany) connected via a 16-bit A/D interface to a pentium IBM clone computer. Before digitization to 5 kHz, the signals are low-pass filtered (1 kHz). Data acquisition and analysis were performed using an ISO-3 multitasking patch-clamp program. For whole cell recordings, the bath was superfused with physiological saline solution (PSS: 130 mM NaCl, 5.9 mM KCl, 2.4 mM CaCl$_2$, 1.2 mM MgCl$_2$, 11 mM glucose, 10 mM HEPES, pH 7.4 with NaOH), and the pipette resistance ranged from 2 to 3 MΩ, and the electrode offset potentials were always zero-adjusted before a Giga-seal is formed. After obtaining a Giga-seal, the membrane under the pipette tip was disrupted by negative pressure so that the whole-cell configuration was established. Afterwards, the membrane capacitance and series resistance were compensated (60–80 %), and whole-cell currents were elicited by applying 300 ms step pulses to potentials ranging from −80 mV to +80 mV in 10 mV increments from a holding potential of −50 mV. Currents were recorded by ISO-3 and saved on the computer for data analysis. Measurements of the whole-cell currents took place at the end of each pulse and were normalized to cell capacitance to calculate the current density (pA/pF) which was then plotted *vs.* the respective voltages, yielding the activation (I/V) curves of the channels in the cell. The SK4 channel blocker, TRAM 34 or clotrimazole were applied to cells by a perfusion pipette. The blocker-sensitive currents were separated from Im as SK4 channel currents (ISK4).

2.12. Circular dichroism (CD)

Far-UV CD spectra were recorded using a Jasco-J-815 device installed with a Peltier controlled cuvette holder (https://jascoinc.com). Spectra were recorded at 10 °C between 260 and 195 nm, data pitch of 0.5 nm and a digital integration time of 2 s, path length of 0.1 cm and a scan speed of 10 nm/s, accumulating 5 scans. For the MT peptide, additional measurements (only from 225 to 220 nm) were performed at a scan speed of 10 nm/s, accumulating 15 scans.

Only measurements at a high tension (HT) voltage below 600 V were included, and identical settings were used to record a spectrum of the buffer, which was then subtracted. Peptide and proteins were dissolved at room temperature in PBS buffer (pH 7.3) and 137 mM NaF at concentrations from 20 to 400 μM. The ellipticity was converted to mean residue weight ellipticity using equation (1).

$$[\theta]_{MRE} = \frac{\frac{MW}{(n-1)} mdeg}{10cd} \tag{1}$$

where $[\theta]_{MRE}$ is the mean residue weight ellipticity, c the concentration in g/L, n the number of residues, d the path length in cm and MW the molecular weight in Da.

To calculate percentage of helicity, equation (2) was used [30].

$$\%Helicity = 100 \frac{[\theta]_{222}}{-40,000\left(1 - \frac{2.5}{n}\right)} \tag{2}$$

where $[\theta]_{222}$ is the MRE at 222 nm and n, the number of peptide bonds. To obtain K_D values, the data was fitted using a biphasic dose response curve (GraphPad Prism software, version 10.1.2, La Jolla, CA), excluding the outlier at 360 μM at 10 °C. Helicity was predicted using the Agadir webserver [31–33] at pH 7.3, ionic strength of 0.137 and 238 K, to mimic CD experiment conditions at 10 °C. No terminal protections were chosen. Far-UV CD spectra of K-RAS FL and K-RAS$_{\Delta HVR}$ in GTP and GDP-loaded states were measured for both WT and G12V isoforms, using identical settings as for the MT peptide and the M7-CC protein, but supplemented with 5 mM MgSO$_4$ to the CD buffer for K-RAS$_{\Delta HVR}$. Protein concentrations ranged from 8 μM to 15 μM.

2.13. Nuclear magnetic resonance (NMR) spectroscopy

NMR samples containing 40–433 μM ^{13}C,^{15}N-M7-CC protein, in the same buffer as the CD samples, were supplemented with 10 % D$_2$O (*v/v*) and 0.7 mM 4,4-dimethyl-4-silapentane-1-sulfonic acid (DSS) as a reference. For interaction studies with FL K-RAS protein variants, the buffer had 20 mM potassium phosphate (pH 7.4), 5 mM MgCl$_2$ and 50 or 150 mM KCl. The interaction with the K-RAS HVR mimicking peptide was probed in the same buffer at 50 mM KCl with 40 μM M7-CC protein and 800 μM HVR peptide. The interaction with the globular domain (GD) of K-RAS (K-RAS$_{\Delta HVR}$) was probed in the same buffer as with the HVR peptide, keeping M7-CC constant at 40 μM and titrating the K-RAS$_{\Delta HVR}$ into it, using concentrations between 80 and 5 μM. All NMR spectra were acquired at 283 K on a Bruker AVANCE III 750-MHz (^{1}H) spectrometer (Billerica, MA), equipped with a cryogenic probe, except for measurements with FL K-RAS protein variants, which were performed at 298 K. For interactions with the K-RAS$_{\Delta HVR}$, the spectra were acquired on a Bruker AVANCE III 600-MHz (^{1}H) spectrometer. Free induction decays were transformed and visualized in NMRPipe [34] or Topspin (Bruker Biospin) and subsequently analysed using the CcpNmr Analysis software [35]. Proton chemical shifts were internally referenced to DSS at 0.00 ppm, with heteronuclei referenced by relative gyromagnetic ratios. Assignments of backbone nuclei of M7-CC were performed manually at 160 μM from the analysis of ^{15}N-^{1}H-HSQC, ^{13}C-^{1}H-HSQC, HNCACB, HNCOCACB and HNCO spectra acquired with nonuniform sampling [36] using standard pulse sequences (BMRB; ID: 52269). Secondary chemical shifts (SCSs) of the M7-CC were calculated

based on C$^\alpha$ shifts and predicted random coil values [37]. To determine the intensity changes, (I/I$_{40μM}$)-ratios were calculated using the intensities of the peaks in the ^{15}N-^{1}H-HSQC at different concentrations relative to 40 μM, as described by equation (3). Intensities at each concentration where internally normalized to the most intense peak from K554 outside the coiled coil (CC) region.

$$I/I_{40\mu M} = \frac{\left(I_{x\,\mu M}^{residue} \middle/ \left(\frac{I_{x\,\mu M}^{K554}}{I_{40\,\mu M}^{K554}}\right)\right)}{I_{40\,\mu M}^{residue}} \tag{3}$$

2.14. Oxidation assay

Two samples of M7-CC protein in CD buffer were prepared at three concentrations: 20 μM, 40 μM and 1000 μM (all in 40 μL). One sample of each concentration was supplemented with 2 μL of H$_2$O$_2$, the other was kept for 4 h in air and was thoroughly mixed. From the latter samples, 20 μL was extracted to generate new samples, to which 1 μL of 1 M DTT was added. All samples were subsequently supplemented with SDS sample buffer and boiled for 5 min at 95 °C, followed by analysis on 15 % (*v/v*) SDS-PAGE gels.

2.15. Computational model of the MTMR7-CC domain dimer

The M7-CC protein sequence was submitted to the CCBuilder web-server, putting the first amino acid at position "a" of the heptad repeat, and setting the oligomeric state as dimer [38]. The resulting M7-CC dimer was then submitted to the YASARA energy minimization server for optimization [39], using the standard settings of the webserver. Structural analysis was performed in the PyMOL Molecular Graphics System (version 2.4.1 Schrödinger, LLC).

2.16. Radiochemistry

A late stage radiofluorination approach was employed to for radiolabelling of the MT peptide with fluorine-18. The prosthetic group, [^{18}F] FPAT, was produced and appended to the MT peptide via potassium acyltrifluoroborate (KAT) ligation as recently described [40]. The identity of [^{18}F]MT was confirmed by co-injection with the corresponding non-radioactive reference MT peptide.

2.17. In vivo positron emission tomography (PET) imaging

Animal care and study procedures were in accordance with the Swiss Animal Welfare legislation. The experiments were authorized by the Veterinary Office of the Canton Zurich, Switzerland. Wistar male rats were acquired from Charles River (Sulzfeld, Germany). Isoflurane was used for anaesthesia, and the rat underwent a 60 min dynamic scan (kidney and liver regions) inside a PET/CT scanner (Super Argus, Sedecal, Madrid, Spain) upon tail-vein injection of 15.49 MBq of the [^{18}F]MT peptide. The PET scan was followed by computed tomography (CT) for anatomical alignment. The scan was analysed using PMOD v4.002 (PMOD Technologies, Zurich, Switzerland). The data was reconstructed in user-defined time frames (voxel size of 0.3875 × 0.3875 × 0.775 mm) as previously described [41].

2.18. Ex vivo biodistribution

[^{18}F]MT peptide was administered to three male Wistar rats (baseline) via tail-vein injection. The animals were anesthetized using isoflurane prior to decapitation at 30, 60 and 90 min, post-injection, respectively (n = 1 per time point). Organs were dissected, weighed, and the radioactivity in each organ was quantified using a γ-counter

(PerkinElmer, Schwerzenbach, Switzerland). The results are reported as % normalized injected dose per g of tissue.

2.19. Statistics and software

Results are means ± S.E. from at least 3 independent experiments from (i) the same cell line from consecutive cultivation passages or (ii) from different individuals (mice). Optical density (O.D.) values from MTT assays were normalized by division through the baseline value, defined as 100 % or -fold 1. The O.D. values from bands in Western blots were normalized to house-keeper proteins (HSP90, Lamin A/C, β-actin) and calculated as -fold of control. The Ct values from RT-qPCRs were normalized to the house-keeper gene (*B2M*) and calculated according to the ΔΔCt method [42].

Statistical analysis was conducted with Graphpad Prism software (version 6.0, La Jolla, CA). Tests were two-sided, and p-values <0.05 considered significant and marked by asterisk (*). Open access web tools were RCSB Protein Data Bank PDB (https://www.rcsb.org), NCBI BLASTp (https://www.ncbi.nlm.nih.gov) and cBioPortal of Cancer Genomics (https://www.cbioportal.org) [43]. Colocalization analysis was performed with ImageJ (imagej.nih.gov/ij) as follows: For RAB5, RAB9, calnexin and pan-RAS using GFP- or FLAG-tagged MTMR7 overexpression, fluorescence intensity (FI) for the indicated Ab was measured in areas with high and low MTMR7 FI. For colocalization of pan-RAS and endogenous MTMR7, Pearson's coefficient of red and green pixel intensities was determined using the JACoP Plugin. The FI thresholds were determined using Costes' automatic threshold algorithm [44]. The correlation diagram was created using the Colocalization Finder plugin.

3. Results

3.1. MTMR7 localizes with endosomal markers at phospholipid-rich membranes

When studied under the microscope, many MTMs appear as sub-membranal cytoplasmic-to-perinuclear "spots/punctae" in the cell, which colocalize with internal membranes (e.g., endosomes) [13]. To address if this was also true for MTMR7, HEK293T cells were transfected for 48 h with an expression plasmid encoding full-length (FL) MTMR7 protein together with GFP-tagged constructs expressing the PH domain of protein kinase B (AKT) or phospholipase delta (PLCδ), respectively. These PH domains served as sensors for PIP-rich membranes. Cells were fixed and stained for immunofluorescence (IF) microscopy. Therein, MTMR7 was visible in the vicinity of the PH-AKT-GFP or PH-PLCδ-GFP domains, but not overlapping with the actin cytoskeleton (**S1**).

To further evaluate the subcellular localization of MTMR7, HCT116 cells, which had been previously evinced to express high levels of endogenous MTMR7 protein [15], were left untreated, while HEK293T cells, which express low levels of endogenous MTMR7 protein [15], were transfected with FLAG-tagged MTMR7 FL plasmid for 48 h. Cells were fixed and stained for IF analysis using Abs against organelle markers. In HCT116 cells, endogenous MTMR7 was found in the cell "body" as small spots/punctae identified as sub-membranal vesicles of late (RAB9+) endosomes (Fig. 1A). Ectopic MTMR7 colocalized with calnexin, a marker for the endoplasmic reticulum (ER) (Fig. 1B) and with early (RAB5+) endosomes (Fig. 1C). These patterns suggested that both endogenous and overexpressed MTMR7 protein are distributed in the cytosol around the endosomal system.

3.2. MTMR7 colocalizes with pan-RAS and reduces GTPase activity in KRAS-mutated cancer cell lines

Several MTMs localize to the endosomal system to alter subcellular traffic of the EGFR [19], and MTMR7 inhibits the downstream RAS-ERK1/2 and PI3K-AKT signaling pathways [15]. We therefore

hypothesized that MTMR7 may negatively regulate p21 RAS GTPases. This idea was consistent with the notion that (i) stability and activity of RAS are dependent on binding to negatively charged phospholipids (e.g. PS) in cellular membranes [10,45] and (ii) MTMR7 dephosphorylates PI (3)P or PI(3,5)P2, thus lowering the richness of negative charges on the membrane inner leaflet. To achieve this effect, MTMR7 and RAS will need to inhabit the same cellular compartment as the endosomes and may interact directly with each other.

To address this, SW480 cells with low expression of endogenous MTMR7 [15] were transfected with GFP-tagged MTMR7 FL plasmid for 48 h followed by IF staining with pan-RAS Ab (Fig. 1D). The fluorescence intensity (FI) of pan-RAS was higher in cellular regions with high MTMR7 levels, suggesting that the two proteins are in vicinity and in compartments imaged by endomembrane markers. To assess the colocalization of endogenous MTMR7 and RAS proteins, IF staining with individual Abs against MTMR7 and pan-RAS was performed in HCT116 cells, which have high endogenous levels of MTMR7. Colocalization analysis was conducted on n = 24 images containing n = 196 cells. Pearson's Coefficient with Costes' automatic threshold algorithm revealed a strong correlation between red (MTMR7) and green (pan-RAS) pixel intensities (r = 0.966 M1 = 0.847 & M2 = 0.986) indicative of a high probability of colocalization (Fig. 1E and F).

To test whether MTMR7 can alter the GTPase activity of RAS proteins, GST-pulldown assays were performed. Human GI cancer cell lines with different *KRAS* mutations (G12V, G12D, G13D) [46] were transfected with empty vector (EV) or MTMR7 FL plasmid for 48 h (Fig. 2A). Total cell lysates were then incubated with recombinant GST-tagged RAL-GDS, a bait for the detection of active GTP-bound pan-RAS (N-RAS, H-RAS, K-RAS). This molecule is a guanine nucleotide dissociation stimulator (GDS) that directly interacts with RAS and functions as a RAS effector molecule. High pan-RAS activity was observed in cancer cell lines from the colorectum (SW480 *KRASG12V*), pancreas (PaTu8902 *KRASG12V*) and stomach (AGS *KRASG12D*) with *KRASG12* mutated alleles and in the CRC cell line HCT116 that harbours a *KRASG13D* mutation. In contrast, *KRAS* wild-type (WT) cells including HEK293T and the two CRC cell lines Caco2 and HT29 had no detectable active GTP-bound RAS, as previously shown [47]. The amount of GTP-bound RAS was significantly reduced after MTMR7 overexpression (Fig. 2A; *p < 0.05 MTMR7 *vs.* EV, One sample *t*-test, n = 3–5 per cell line). Thus, in summary, MTMR7 localizes to endosomal membranes and co-localizes with pan-RAS. Furthermore, overexpression of MTMR7 reduces GTPase activity in human *KRAS*-mutated cancer cell lines.

3.3. MTMR7 inhibits EGF-stimulated ERK1/2 signaling

To study the impact of MTMR7 overexpression on the EGFR-RAS-ERK1/2 signaling, cells (SW480, HEK293T) were transfected with EV or MTMR7 FL plasmid for 48 h, followed by an overnight (~16 h) serum-deprival and subsequent stimulation with EGF (50 ng/mL) for 0–30 min (Fig. 2B). Consistent with previous results using insulin [15], MTMR7 overexpression reduced the phosphorylation of ERK1/2 compared to EV control (O.D. at time point = 5 min: EV 3.5 ± 0.4 *vs.* MTMR7 1.6 ± 0.5*10^7, *p = 0.044, *t*-test; n = 3 per cell line).

We next asked if inhibition of the RAS-ERK1/2 cascade by MTMR7 propagates to a reduction of down-stream transcriptional events in the nucleus. The serum-response-element (SRE) is a *cis*-acting DNA motif located in enhancers and promoters of immediate-early genes. It drives transcription of these genes (e.g. *c-FOS*) upon activation of the RAS-ERK1/2 pathway by mitogenic stimuli (e.g. EGF, serum) [48]. To assess the effect of MTMR7 overexpression on the transcriptional activity of this pathway, HEK293T cells were co-transfected with a luciferase reporter plasmid harbouring the SRE of the human c-*FOS* promoter together with EV or MTMR7 FL plasmid, respectively, followed by a 48 h incubation with or without fetal calf serum (FCS, 20 % *v/v*) as a mitogenic stimulus. MTMR7 overexpression significantly lowered the SRE-driven luciferase activity in total cell lysates in absence (by 85 ± 3
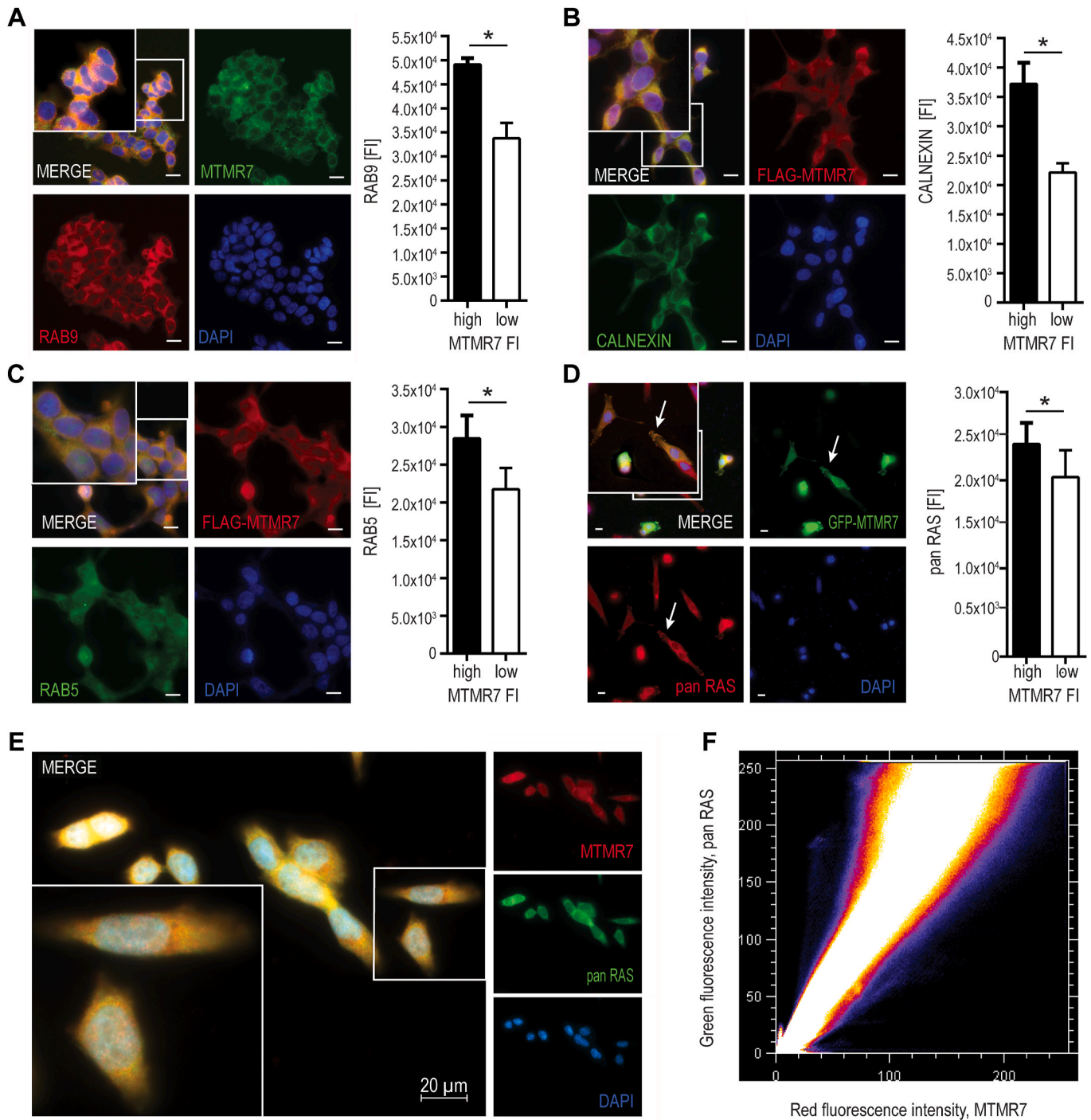
Fig. 1. Subcellular localization of MTMR7. **A, MTMR7 colocalizes with late endosomes.** Immunofluorescence (IF) staining was performed in HCT116 cells (with high endogenous MTMR7 protein) using Abs against MTMR7 and RAB9 (late endosome marker). Quantification of stained slides revealed a higher RAB9 fluorescence intensity (FI) in cellular regions with high MTMR7 FI. Data are means of absolute FI ± S.E. (n = 6 fields, *p = 0.0051 MTMR7 high *vs.* low FI, paired *t*-test, n = 2). Colour legend: green = MTMR7, red = RAB9, blue = nuclei (DAPI); original magnification 630x, Scale bar = 10 μm. **B-C, MTMR7 also colocalizes with the ER and early endosomes.** HEK293T cells (with low endogenous MTMR7 protein) were transfected with FLAG-tagged MTMR7 full-length (FL) plasmid for 48 h, followed by IF staining with calnexin (**B**) or RAB5 (**C**). Increased FI for calnexin (ER marker) and RAB5 (early endosome marker) was detected in cellular regions with high MTMR7 FI as compared to regions with low MTMR7 FI. Data are means of absolute FI ± S.E. (panel B: n = 6 fields, *p = 0.0049; panel C: n = 5 fields, *p = 0.0171; MTMR7 high *vs.* low FI, paired *t*-test, n = 2). Colour legend: green = Calnexin/RAB5, red = FLAG-MTMR7, blue = nuclei (DAPI); original magnification 630x, Scale bar = 10 μm. **D, MTMR7-GFP colocalizes with RAS proteins.** SW480 cells (with low endogenous MTMR7 protein) were transfected with GFP-tagged MTMR7 FL plasmid for 48 h, followed by IF staining with pan-RAS p21 Ab. The RAS FI was higher in cellular regions with high MTMR7 FI. Data are means of absolute FI ± S.E. (n = 13 fields, *p = 0.0297 MTMR7 high *vs.* low FI, paired *t*-test, n = 2). Colour legend: green = GFP-MTMR7, red = pan-RAS, blue = nuclei (DAPI); original magnification 400x, Scale bar = 10 μm. **E-F, Endogenous MTMR7 colocalizes with RAS proteins.** HCT116 cells (with high endogenous MTMR7 protein) were subjected to IF staining with MTMR7 and pan-RAS p21 Abs. (**E**) Representative images. Colour legend: green = pan-RAS, red = MTMR7, blue = nuclei (DAPI); original magnification 630x, Scale bar = 20 μm. (**F**) Correlation diagram of red (MTMR7) and green (pan-RAS) pixel intensities of n = 24 images containing n = 196 cells (r = 0.966 M1 = 0.847 & M2 = 0.986).
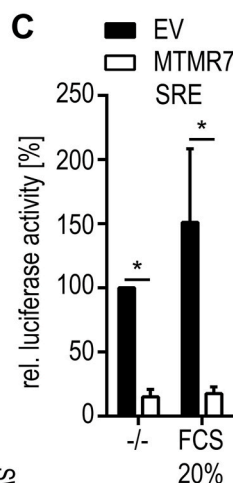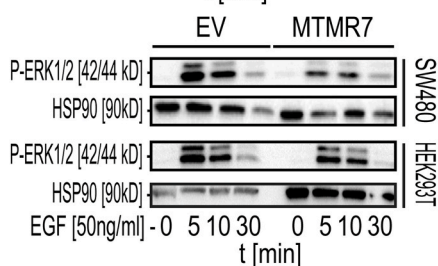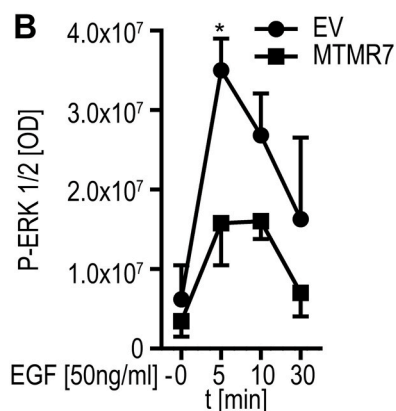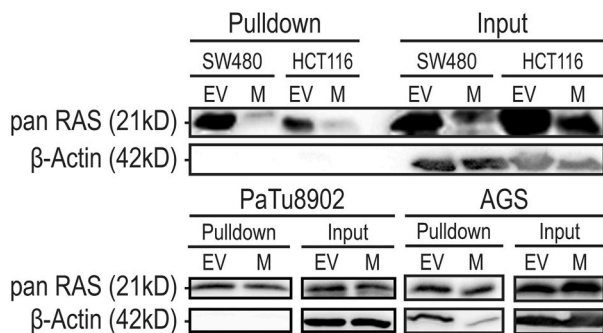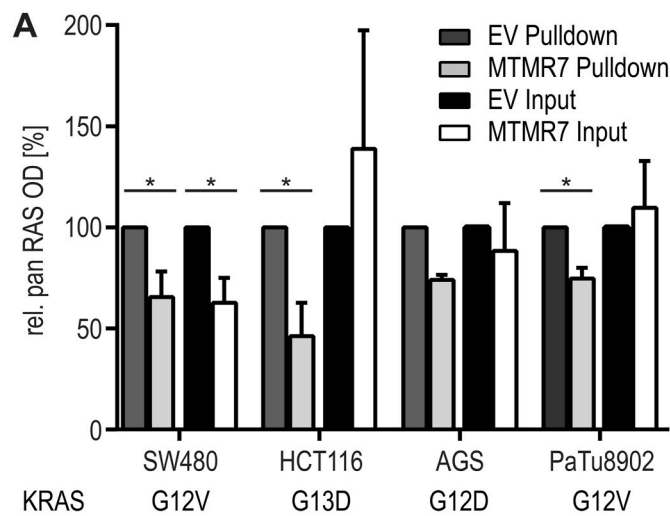
Fig. 2. MTMR7 inhibits RAS signaling. **A, MTMR7 reduces RAS GTPase activity and pan-RAS protein levels.** *KRAS*-mutated GI cancer cell lines (SW480, HCT116, PaTu8902, AGS) were transfected with empty vector (EV) or MTMR7 FL plasmid for 48 h, followed by GST-pulldown from total cell lysates using RAL-GDS as a bait for precipitation of active GTP-bound RAS proteins, which were then detected by Western blot with pan-RAS p21 Ab (specific for N-, H- and K-RAS). ERK1/2 or β-actin were not (except for AGS) precipitated by RAL-GDS and served as a control for equal loading (input). Representative images and quantifications. O.D. values from band in gels are calculated as % ± S.E. (*p < 0.05 MTMR7 *vs.* EV, One sample *t*-test, n = 3–5 per cell line). **B, MTMR7 inhibits EGF-stimulated ERK1/2 signaling.** Cells (SW480, HEK293T) were transfected with EV or MTMR7 FL plasmid for 48 h, followed by serum-deprival for overnight (~16 h), and were then stimulated with EGF (50 ng/mL) for 0–30 min. Representative Western blots and quantitative analyses from total cell lysates. O.D. values from bands in gels are means ± S.E. (at time point = 5 min: *p = 0.044 MTMR7 *vs.* EV, *t*-test, n = 3 per cell line). **C, MTMR7 inhibits *c-FOS* promoter transcription.** HEK293T cells were co-transfected with SRE-driven *c-FOS* luciferase reporter gene plasmid together with EV or MTMR7 FL and incubated in absence (−/−) or presence of FCS (20 % *v/v*) for 48 h. Luciferase activity in total cell lysates was normalized to the protein content and calculated as % ± S.E. compared with day 0 (*p < 0.05 MTMR7 *vs.* EV, 2wayANOVA, Bonferroni's multiple comparisons test, n = 3).

%) or presence (by 133 ± 33 %) of FCS (*p < 0.05 MTMR7 *vs.* EV, 2wayANOVA, Bonferroni's multiple comparisons test, n = 3) (Fig. 2C). Thus, MTMR7 inhibits ERK1/2 signaling, resulting in lowered transcriptional activity of immediate early genes relevant for cancer cell proliferation.

3.4. MTMR7 redistributes RAS at cellular membranes through electrostatic effects

To address if MTMR7 affects the level and subcellular distribution of RAS, cells (HCT116, SW480, HEK293T) were transfected with EV or MTMR7 FL plasmid for 48 h, serum-deprived for overnight, followed by stimulation with FCS (20 % *v/v*) for 0–180 min before subcellular fractionation (SCF). Western blot analyses demonstrated that MTMR7 overexpression exerted a trend for decreased pan-RAS protein levels in the insoluble fraction (~10–30 %) which contained cytoskeleton, matrix and membrane proteins (HCT116: p = 0.0467 EV *vs.* MTMR7, 2wayANOVA, n = 3 per cell line) (S2). However, no translocation of RAS protein to the soluble, cytosolic fraction was observed.

To substantiate these findings, we performed IF microscopy on SW480 cells, which were transfected with GFP-tagged MTMR7 FL plasmid for 48 h before fixation and staining. The FI of pan-RAS protein was reduced at the cellular periphery in GFP positive MTMR7-transfected cells compared to GFP negative cells (*p < 0.05 GFP + *vs.* GFP-, *t*-test, n = 3) (Fig. 3A). This data confirmed that MTMR7 overexpression lowers the recruitment of RAS proteins to cellular membranes.

Previous studies have shown that changing the electrostatic membrane potential results in detachment of RAS proteins from cellular membranes with subsequent inactivation in the cytosol [9]. Specifically, potassium chloride (KCl) triggers rapid depolarisation of the plasma membrane [9], resulting in fewer negative charges at the inner leaflet of the membrane. This again reduces the electrostatic forces for binding of the positively charged lysine-rich HVR of K-RAS4B, the major oncogenic variant in cancers [10]. We therefore tested the impact of MTMR7 on the amount of pan-RAS protein at cell membranes in the presence KCl.

To this end, HEK293T cells were transfected with EV or MTMR7 FL plasmid for 48 h, followed by an overnight serum-deprival and subsequent incubation with 50 mM KCl for 0–30 min. Western blot analyses on total cell lysates revealed that, upon MTMR7 overexpression, KCl reduced pan-RAS protein levels within 0–5 min by 20–25 % compared to the EV control. After 30 min, KCl further reduced RAS protein to the level of the MTMR7-transfected cells (*p < 0.05 MTMR7 *vs.* EV, 2wayANOVA, Bonferroni's multiple comparisons test, n = 3) (Fig. 3B, left).
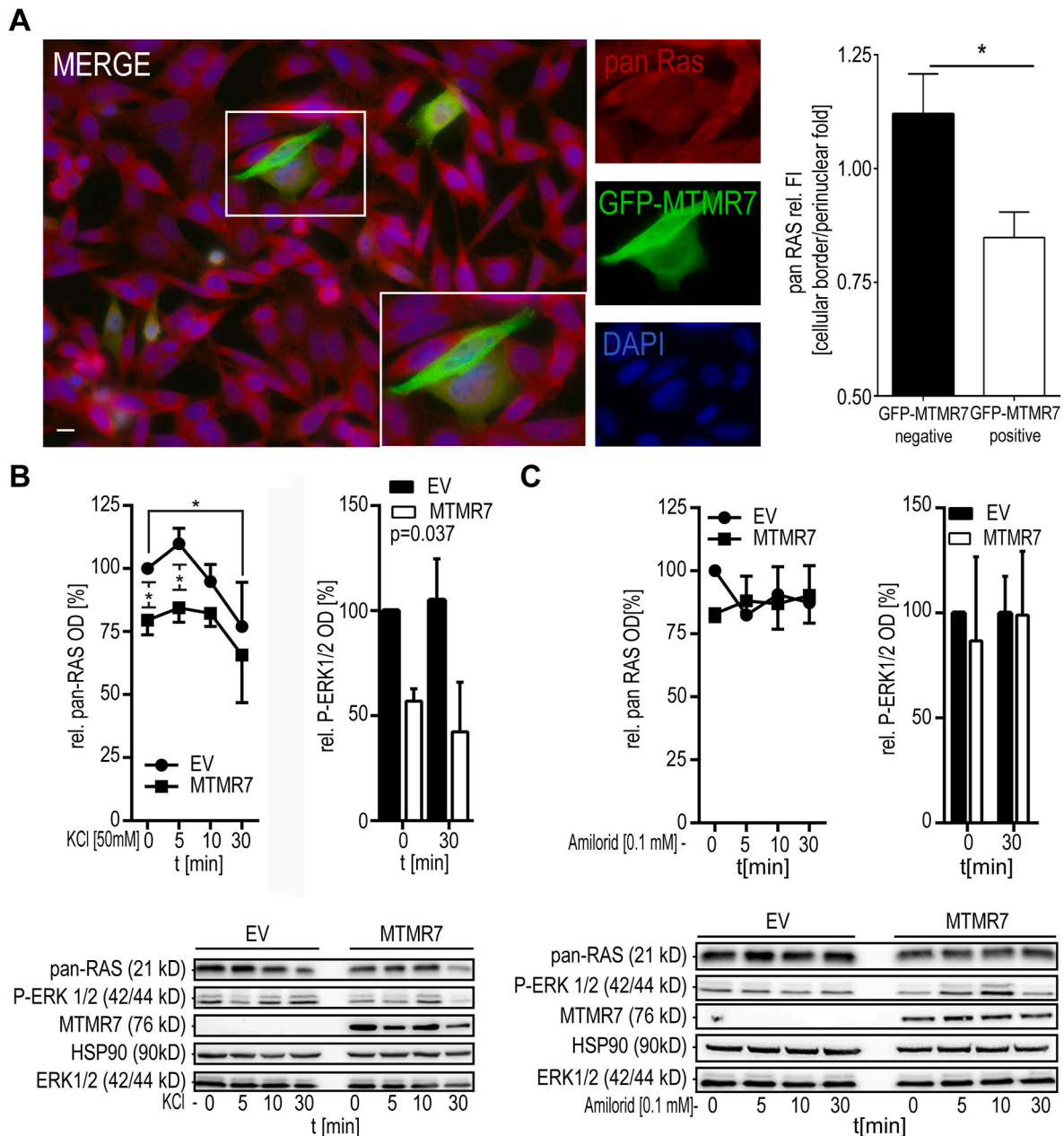
Fig. 3. MTMR7 inhibits binding of RAS to membranes. **A, MTMR7 reduces membrane localization of RAS proteins.** SW480 cells were transfected with GFP-MTMR7 FL plasmid for 48 h before IF microscopy. Fluorescence intensity (FI) was measured at the cellular periphery and the perinuclear region. Given are the ratios between the peripheral and perinuclear RAS FI. Note that the FI for RAS was reduced in single GFP-MTMR7 FL positive cells (white square). Data are mean relative FI ± S.E. (*p < 0.05 GFP + vs. GFP-, t-test, n = 3). Colour legend: red = pan-RAS p21 Ab, green = GFP, blue = nuclei (DAPI); Original magnification 400x, Scale bar = 10 μm. **B, MTMR7 reduces RAS protein upon membrane depolarisation by KCl.** HEK293T cells were transfected with EV or MTMR7 FL plasmid for 48 h, followed by an overnight serum-deprival and subsequent incubation with 50 mM KCl for 0–30 min. Representative images and quantitative analyses from Western blots on total cell lysates. O.D. values were calculated as % ± S.E. of untreated EV control (*p < 0.05 MTMR7 vs. EV, 2wayANOVA, Bonferroni's multiple comparisons test, n = 3). **C, MTMR7 does not reduce RAS protein upon membrane hyperpolarisation by Na + channel blocker amiloride.** HEK293T cells were transfected as in B and subsequently incubated with 0.1 mM amiloride for 0–30 min. Representative images and quantitative analyses from Western blots. O.D. values were calculated as % ± S.E. of untreated EV control (n.s. MTMR7 vs. EV, 2wayANOVA, Bonferroni's multiple comparisons test, n = 3).

In contrast to KCl, blockage of inward sodium ion channels, by e.g., amiloride, induces rapid hyperpolarisation of the plasma membrane, resulting in more negative charges at the inner leaflet of the phospholipid bilayers, thus enhancing the electrostatic forces for binding of the HVR of K-RAS4B to membranes. Previous studies have shown that this leads to pronounced recruitment and activation of membrane-bound RAS [9]. We therefore tested Na+ channel blockage as above for KCl. HEK293T cells were transfected with EV or MTMR7 FL plasmid, respectively, and treated with or without amiloride (0.1 mM) for 0–30

min. Western blot analysis on total cell lysates demonstrated that MTMR7 failed to reduce pan-RAS protein in presence of amiloride (Fig. 3C, left). Western blotting also confirmed that in MTMR7-transfected cells phosphorylation of ERK1/2 was reduced by KCl (Fig. 3B, right) but not by amiloride (Fig. 3C, right).

Taken together, MTMR7 reduces the amount of RAS protein at cellular membranes. Moreover, membrane depolarisation imitates the effect of MTMR7 overexpression, whereas membrane hyperpolarisation reverses it. These findings suggest that electrostatic interactions could

play a role in inhibition of RAS by MTMR7. However, which domains in the two proteins account for their interaction remained elusive.

3.5. The enzymatic activity of MTMR7 is dispensable for RAS inhibition

To characterise the protein domain(s) in MTMR7 responsible for the observed effects on RAS, we asked whether inhibition of downstream ERK1/2 signaling depends on the enzymatic activity of the catalytical (HCS) domain of MTMR7, and hence the cellular PI(3)P pool. HEK293T cells were transfected with the SRE reporter together with EV or MTMR7 FL plasmid for 6 h, then serum-starved overnight and stimulated with FCS (20 % *v/v*) for additional 48 h. In addition, PI(3)P was depleted using 1 μM of the PIK3C3/VPS34 inhibitor SAR405. Notably, PI(3)P depletion had no effect on the transcriptional activity of the SRE **(S3)**. Thus, the enzymatic activity of MTMR7 seems dispensable for inhibition of the RAS-ERK1/2 pathway.

3.6. The charged CC domain of MTMR7 is disordered and a candidate for RAS interaction

We next focused on the C-terminal domain of MTMR7, searching for highly charged regions. Using IDDomainSpotter [49] **(S4)**, we observed that the CC domain harbours both highly negatively and highly positively charged regions (Fig. 4A). The CC domain is responsible for heterodimerization with MTMR9, which in turn enhances the phosphatase activity of MTMR7 [12]. Therefore, this domain may be a candidate for the interaction with RAS proteins.

The fragmental structures of some MTMs have been solved, but not that of MTMR7, and the CC domain was never included in any structural analyses due to its disorder [50]. We produced the CC domain (M7-CC, aa 514-554) as a recombinant protein in bacteria and compared its properties to the myristoylated MT peptide used in our previous study [14]. To improve purification, we added seven and four N- and C-terminal flanking residues, respectively (Fig. 4B).
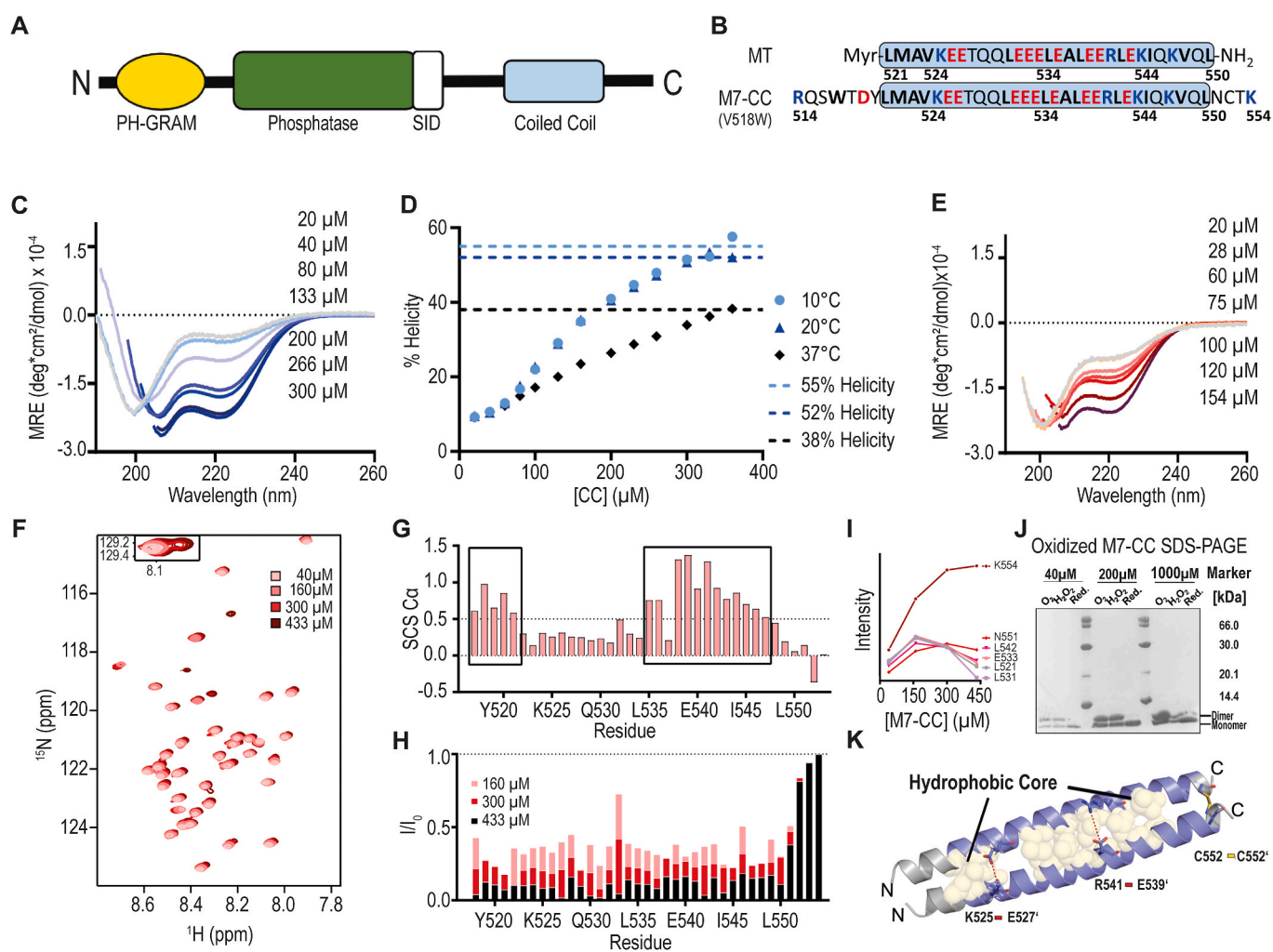

Fig. 4. MT peptide and MTMR7 coiled coil domain (M7-CC) are disordered and can form helical dimers. **A,** Domain structure of MTMR7 FL enzyme. **B,** Sequences of the MT peptide and the M7-CC domain with numbering as in MTMR7 FL protein. Hydrophobic residues are in black and bold, basic residues in blue and acidic residues in red. MT is myristoylated at the N-terminus (Myr) and amidated at the C-terminus. Blue boxes mark the canonical CC domain aa sequence of MTMR7. **C,** Secondary structure of MT as a function of concentration measured by far-UV CD. **D,** Percentage helicity of MT as a function of concentration calculated from $\theta_{222\ nm}$ at different temperatures. **E,** Secondary structure of M7-CC as a function of concentration measured by far-UV CD. **F,** ^{15}N,^{1}H-HSQCs of increasing concentrations of ^{15}N -M7-CC. **G,** SCS of C$^{\alpha}$-atoms as a function of sequence (M7-CC at 160 μM). Boxes mark transient helical regions. **H,** Peak intensity ratios at different M7-CC concentrations relative to the intensity at 40 μM, normalized to the intensity of K554. **I,** Non-normalized intensity changes of selected residues. **J,** SDS PAGE gel of M7-CC in oxidizing and reducing conditions at increasing concentrations. **K,** Cartoon representation of the model of the M7-CC parallel dimer stabilized by a cysteine bridge (shown as sticks). The canonical CC region is coloured in blue. Potential salt bridges are shown as dashed line, the hydrophobic core as transparent yellow spheres.

Far-UV circular dichroism (CD) spectroscopy on the myristoylated MT revealed that the peptide adopted a largely disordered structure at low concentrations. Notably, its helicity increased with higher peptide concentrations (Fig. 4C). At all temperatures tested, the peptide had a helical content of ~9 % at the lowest concentration, matching the ~12 % predicted by Agadir [31–33]. Helicity increased with elevated peptide concentration to 55 %, 52 % and 38 % at 10 °C, 20 °C and 37 °C, respectively (Fig. 4D), and occurred in an apparent three-state reaction, where the helicity first reached a plateau and then continued to increase under continued peptide addition. For each dataset, two K_d values were extracted giving K_d values of 130–157 μM and 250–340 μM, respectively. A comparable behaviour was observed for the recombinant M7-CC protein (Fig. 4E). This observation underscored its validity as a model for the MT peptide, despite being longer and not lipidated. In the M7-CC protein, helicity rose from 23 % to 56 % when the concentration was increased from 20 μM to 154 μM. This data shows that the MTMR7-CC domain can dimerize and likely also form higher order structures.

3.7. Monomeric MTMR7-CC directly interacts with the globular domain of K-RAS

To enable interaction analyses with K-RAS, we used nuclear magnetic resonance (NMR) spectroscopy. The NMR chemical shifts of all but the three N-terminal residues of the $^{15}N,^{13}C$-M7-CC protein were assigned at a final concentration of 160 μM (BMRB, ID: 52269). The secondary structure content was derived from the secondary chemical shifts (SCSs) of the C^α atoms revealing two transient helical stretches with consecutive positive values: One N-terminally of the canonical CC sequence (W517-L521) and one in its C-terminal half (L535-K547) (Fig. 4G). The overall helical content based on NMR shifts was 17 %, corresponding to the disordered monomer observed by CD.

Increasing the concentration of M7-CC led to consistent loss of NMR peak intensity covering the entire peptide (Fig. 4F, H-I), indicating a chemical exchange with an 'NMR-invisible' state. Above a concentration of 160 μM, four new peaks emerged, identified as the four C-terminal residues including the C552 residue. The increase in helicity observed in CD, along with the reduction of NMR peak intensities, suggested that the M7-CC domain formed concentration-dependent oligomers of higher helicity than the disordered monomers. To investigate whether parallel or anti-parallel dimers formed, we exploited the C-terminal C552 residue. In parallel dimers, the C552 would form a disulphide bond at oxidizing conditions. M7-CC at different concentrations were oxidized with air or H_2O_2, then analysed by SDS-PAGE and compared to reduced samples (Fig. 4J). Only the monomer band was visible in all reduced samples. For all oxidized samples, two bands were visible, one of the monomer and one of a higher mass, corresponding to a dimer. A model of a parallel M7-CC dimer was then built using CCBuilder and optimized using the YASARA webserver (Fig. 4K). As depicted, the structure is stabilized by a hydrophobic core of leucines and isoleucines and by salt bridges between the residues E539 and R541 and K525 and E527, located in positions "e" and "g" of the heptad repeat.

To address a direct interaction between MTMR7-CC and K-RAS, we produced the K-RAS WT and the K-RAS^{G12V} variant as recombinant proteins, both as FL enzyme and as the globular domain (GD), which lacked the HVR (ΔHVR). After confirming the folding of K-RAS and K-RAS^{G12V} by CD (**S5**), these proteins were loaded with different nucleotide cargo (GDP and the non-hydrolysable GTP analogue GTPγS) and added individually to the ^{15}N-M7-CC domain. NMR chemical shift perturbations (CSPs) and changes in peak intensities as a function of the K-RAS concentration were then compared with an NMR spectrum of the ^{15}N-M7-CC domain without K-RAS.

For both K-RAS variants, the FL protein interacted only weakly with the M7-CC domain, as evident from the subtle CSPs shown in Fig. 5A (left). To test whether those weak interactions may occur in presence of the HVR, we added a K-RAS HVR mimicking peptide to the ^{15}N-M7-CC

protein. However, this interaction was even weaker than the one observed with the FL protein (Fig. 5A, right), and only visible at a 20-fold molar excess of the peptide. This result suggested that the HVR hinders rather than facilitates the interaction of M7-CC with FL K-RAS. We therefore intended to detach the HVR from the GD of the FL WT protein by increasing the salt concentration from 50 to 150 mM. Under these conditions, we observed binding of the M7-CC domain to the GDP-loaded FL K-RAS^{WT} protein, but not to its GTP-loaded state (**S6**).

To elucidate this in detail, the interactions of the M7-CC domain with the ΔHVR protein variants of K-RAS^{WT} and K-RAS^{G12V} were probed in the GDP and GTP-loaded states, respectively. A loss of NMR peaks and large CSPs was already visible at a low molar ratio (1:2) of M7-CC and K-RAS$_{\Delta HVR}$ proteins (Fig. 5B). Plotting the intensity loss per residue (Fig. 5C) revealed that both K-RAS variants interacted with the M7-CC domain via the same two interaction sites (IA1 and IA2) on MTMR7. IA1 included residues T518 – E527 and IA2, A537 – Q546. The strongest overall intensity loss was observed for the GDP-loaded K-RAS^{WT}, the weakest for the GTP-loaded K-RAS^{G12V} variant. This finding suggests a direct interaction between the M7-CC domain and the GD of K-RAS$^{WT/G12V}$, whereas the HVR of K-RAS hinders the interaction. Thus, in summary, the MTMR7-CC domain exists as a disordered monomer at low concentrations and can form a parallel helical dimer at higher concentrations. Both the N- and the C-terminal ends of the MTMR7-CC domain directly interact with the GD of K-RAS$^{WT/G12V}$ and prefer the GDP-bound over the GTP-bound states.

3.8. The MT peptide inhibits proliferation of KRAS-mutated cancer cells in vitro

Based on the direct interaction of K-RAS with the M7-CC domain observed by NMR, we next asked whether the synthetic MT peptide can phenocopy the effect of the MTMR7 FL enzyme in cancer cells. Four human cancer and HEK293T cell lines were cultured for 48 h in the presence of increasing concentrations of MT peptide, and the viability was measured by MTT assay (Fig. 6A). IC$_{50}$ values were extracted from sigmoidal dose-response curves (HCT116: 0.1 μM; HEK293T: 0.13 μM; AGS: 0.11 μM; SW480: 0.12 μM). Time-dependent responses were measured over 24–72 h in the presence of MT or a scrambled control (SC) peptide (both at 1 μM), and viability measured as in A (Fig. 6B and C). Compared with the SC peptide, the MT peptide inhibited cell growth within 48–72 h in SW480 (by 166 ± 46 %), HCT116 (220 ± 65 %), AGS (94 ± 24 %), PaTu8902 (105 ± 21 %) and HEK293T (59 ± 25 %) (*p < 0.05 MT *vs.* SC, 2wayANOVA, Bonferroni's multiple comparisons test, n = 3–5 per cell line). Thus, the MT peptide mimics growth inhibition in the same set of cell lines as achieved before by overexpression of the MTMR7 FL enzyme [15].

3.9. The MT peptide inhibits EGF-stimulated ERK1/2 signaling

To explore if the MT peptide also phenocopies inhibition of RAS-ERK1/2 signaling exerted by the MTMR7 FL enzyme, the cell lines (SW480, HCT116, HEK293T) were incubated with MT or SC peptide (both at 1 μM) for 24 h, followed by serum deprivation overnight and subsequent stimulation with EGF (50 ng/mL) for 0–30 min. Western blot analyses on total cell lysates showed a reduced phosphorylation of ERK1/2 in all cell lines tested (*p < 0.05 MT *vs.* SC, 2wayANOVA, Bonferroni's multiple comparisons test, n = 3 per cell line) (Fig. 6D). However, no effect on the phosphorylation of AKT was seen (**S7**), indicating that the peptide cannot substitute for all modes of action exerted by the FL enzyme.

To analyse whether the observed effects of the MT peptide on signaling close to cell membranes would be propagated to the transcriptional machinery in the nucleus, the cell lines (SW480, HCT116, HEK293T) were transfected with the *c-FOS* SRE luciferase reporter gene plasmid and treated with MT or SC peptide (both at 1 μM) for 24–48 h, respectively. All cell lines displayed a reduced activity of the c-*FOS*
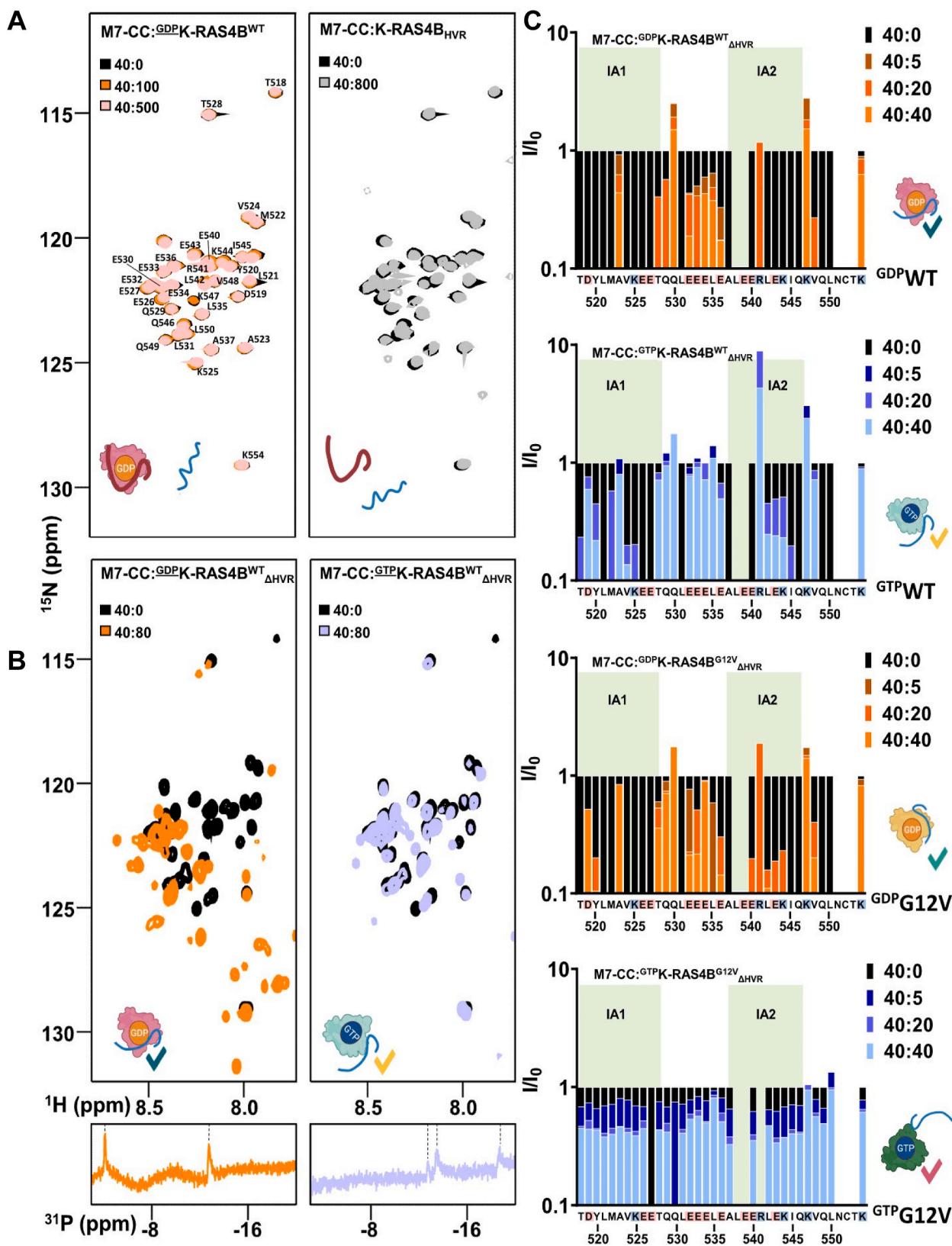
Fig. 5. M7-CC directly interacts with K-RAS. **A,** $^{15}N,^{1}H$-HSQC of ^{15}N-M7-CC alone and with GDP-loaded FL K-RAS^{WT} at ratios of 1:2.5 and 1:12.5 (left) and ^{15}N-M7-CC alone and with the HVR of K-RAS4B at a ratio of 1:20 (right). **B,** $^{15}N,^{1}H$-HSQC of ^{15}N-M7-CC alone and with GDP- (left) and GTPγS-bound (right) K-RAS$_{\Delta HVR}$ at a ratio of 1:2. Below the respective $^{15}N,^{1}H$-HSQC-spectrum, a section of a^{31}P-1D-spectrum is shown, confirming the nucleotide cargo of the respective K-RAS$_{\Delta HVR}$. **C,** Peak intensities plotted as a function of the M7-CC sequence for titrations of the ^{15}N-M7-CC with, from top to bottom: GDP-bound K-RAS$_{\Delta HVR}^{WT}$, GTPγS-bound K-RAS$_{\Delta HVR}^{WT}$, GDP-bound K-RAS$_{\Delta HVR}^{G12V}$ and GTPγS-bound K-RAS$_{\Delta HVR}^{G12V}$. Protein/Peptide graphics were generated using biorender.com.
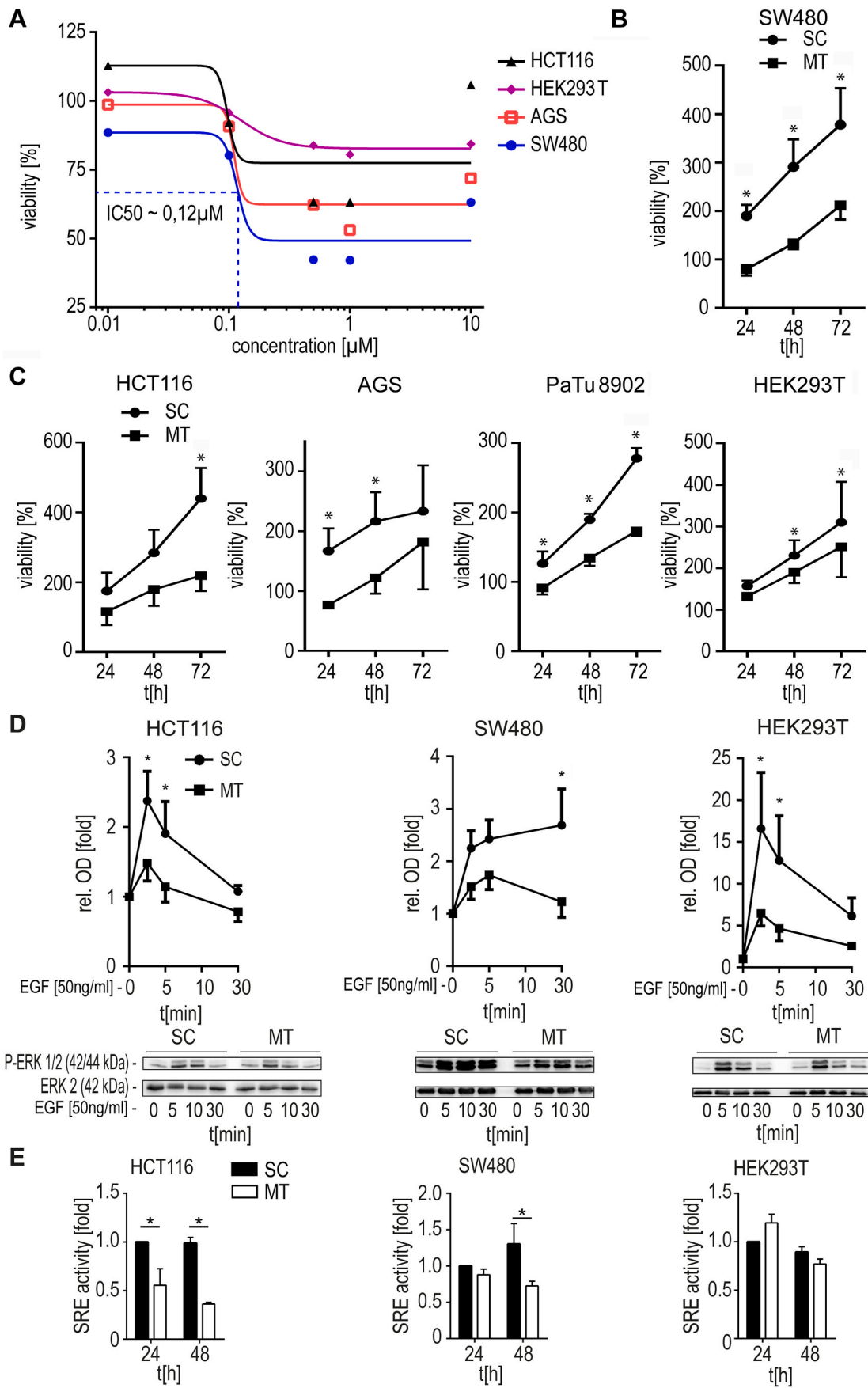
Fig. 6. MT peptide phenocopies MTMR7 FL on RAS inhibition. **A, MT peptide reduces proliferation of human *KRAS*-mutated cancer cell lines.** Concentration-dependent growth inhibition. Cells (HCT116, HEK293T, AGS, SW480) were treated with the concentrations indicated of the MT peptide. Viability was measured by MTT assay after 48 h. O.D. values were calculated as % viability ± S.E. compared with day 0. Curve fitting to sigmoidal dose response was done with Graphpad Prism software (HCT116: $IC_{50} = 0.1$ μM, Hill slope ∼ −11.86, n = 3; HEK293T: $IC_{50} = 0.13$ μM, Hill slope ∼ −2.5, n = 5; AGS: $IC_{50} ∼ 0.11$ μM, Hill slope ∼ −13.20, n = 3; SW480: $IC_{50} ∼ 0.12$ μM, Hill slope ∼ −8.73, n = 3). **B-C, Time-dependent growth inhibition.** Cells (SW480, HCT116, AGS, PaTu8902, HEK293T) were treated with MT or scrambled control (SC) peptide (both at 1 μM) for the indicated time periods. Data were calculated as in A (*p < 0.05 MT *vs.* SC, 2wayANOVA, Bonferroni's multiple comparisons test, n = 3 per cell line; HEK293T: n = 5). **D, MT peptide lowers EGF-mediated ERK1/2 signaling.** Cells (HCT116, SW480, HEK293T) were incubated with MT or SC peptides (both at 1 μM) for 24 h, followed by serum deprival for overnight and subsequent stimulation with EGF (50 ng/mL) for 0–30 min. Representative images and quantitative analyses from Western blots. O.D. values from phosphorylated (P)-ERK1/2 were normalized to general ERK2 and calculated as -fold ± S.E. compared to the corresponding time point = 0 values (*p < 0.05 MT *vs.* SC, 2wayANOVA, Bonferroni's multiple comparisons test, n = 3 per cell line). **E, MT peptide inhibits *c-FOS* promoter transcription.** Cells (HCT116, SW480, HEK293T) were transfected with SRE-driven *c-FOS* luciferase reporter plasmid together with MT or SC peptide (both at 1 μM). After 24 and 48 h, luciferase activity in total cell lysates was measured, normalized to the protein content and calculated as -fold ± S.E. compared with day 0 (*p < 0.05 MT *vs.* SC, 2wayANOVA, Bonferroni's multiple comparisons test, n = 3 per cell line).

promoter upon treatment with the MT compared with the control peptide (*p < 0.05 MT *vs.* SC, 2wayANOVA, Bonferroni's multiple comparisons test, n = 3 per cell line) (Fig. 6E). Conclusively, we found that the MT peptide can mimic the effects of the MTMR7 FL enzyme, confirming the CC domain as the active region of MTMR7 responsible for inhibition of RAS-mediated signaling *in vitro*.

3.10. The MT peptide reduces proliferation of murine GI cancer in vivo

We finally assessed whether the MT peptide also inhibits tumour growth *in vivo*. To determine its biodistribution in tissues, the MT peptide was labelled with ^{18}F-radionuclide and injected (i.p.) into Wistar rats. Positron emission tomography (PET) imaging revealed a strong signal in the liver and the intestinal tract (Fig. 7A). An *ex vivo* biodistribution analysis was performed after 30, 60 and 90 min post injection. This analysis confirmed the data acquired by PET and additionally showed an accumulation of the ^{18}F-radionucleide in the urinary tract indicative of renal excretion (**S7**).

We then resorted to an established mouse model of gastric cancer. The *CEA424-SV40* TAg transgenic C57BL/6J mice express the viral oncogene SV40 large T-antigen (TAg) driven by a promoter derived from the human carcinoembryonic antigen (*CEA*) gene. They develop rapid-onset, highly proliferative intraepithelial carcinomas in the pyloric region of the stomach and the upper duodenum with 100 % penetrance [25].

For experimental studies, female animals (2 months of age, average body weight 20 g) were randomized into treatment and control groups (n = 4–8 per group). Mice were either left untreated (UT), injected with vehicle (VC) alone or with peptides (MT or SC) dissolved in DMSO/PBS and administered i.p. as a single dose of 30 mg/kg per day, 4 times per week for 2 weeks. First, formalin-fixed paraffin-embedded (FFPE) tissue sections from explanted stomachs were stained with haematoxylin and eosin (H&E) dyes and subjected to histopathological analysis (Fig. 7B). 2D quantification of the tumour areas in the pylorus and the upper duodenum showed that the MT peptide decreased the tumour area by 33 ± 9 % compared to mice treated with the SC peptide (*p < 0.05 *vs.* MT, 1wayANOVA, Holm-Sidak's multiple comparisons test, n = 4–8 mice per group). Thus, the MT peptide can reduce tumour growth *in vivo*.

To critically test this finding, *in situ* detection of gastric tumours in mouse stomachs was performed using magnetic resonance imaging (MRI) (Fig. 7C and D) [51]. Mannitol was instilled into the upper GI tract *post mortem* and followed by acquisition of T1/T2 and diffusion weighted images from the anatomic region comprising stomach, pylorus and duodenum. Overall, the MT peptide decreased the tumour volume by 21 ± 9 % compared to the vehicle control (VC) (n = 3 mice per group). Immunohistochemistry (IHC) detecting the proliferation marker Ki67 demonstrated that the number of Ki67+ cells was lowered by 62 ± 17 % upon treatment with the MT peptide compared with the SC peptide (*p < 0.05 *vs.* MT, 1wayANOVA, Holm-Sidak's multiple comparisons test, n = 4–8 mice per group) (Fig. 7E). This data indicated a reduced proliferation of tumour cells upon administration of the MT peptide.

Upon activation, ERK1/2 translocate to the nucleus [52]. Therefore, the fraction of cells positive for nuclear ERK1/2 staining can be used as a surrogate marker for ERK1/2 signaling activity. To assess if the MT peptide exerts its inhibitory effects on the RAS-ERK1/2 cascade also *in vivo*, we performed IHC detecting ERK1/2. Positivity for nuclear ERK1/2 was decreased by 35 ± 16 % as compared to the SC peptide (*p < 0.05 *vs.* MT, 1wayANOVA, Holm-Sidak's multiple comparisons test, n = 4–8 mice per group) (Fig. 7F), a finding which is indicative of inhibition of the RAS-ERK1/2 pathway by MTMR7 *in vivo*. Consistent with the previous Western blot analyses *in vitro* (**S7**), the MT peptide also failed to inhibit the AKT pathway *in vivo*. This conclusion was drawn upon quantification of IHC staining against the phosphorylated S6 ribosomal protein (S6RP), a major downstream target of PI3K-AKT-S6 kinase signaling (**S7**).

To test whether inhibition of ERK1/2 signaling can also be achieved in a mouse model of colorectal carcinogenesis, 11 weeks old C57BL/6J *Apc^{min/+}* mice were treated with MT peptide or VC as indicated above. The positivity for nuclear ERK1/2 was again decreased by 47 ± 7 % as compared to the VC (*p < 0.05 *vs.* MT, *t*-test, n = 5 mice per group) (Fig. 7G), confirming the inhibition of ERK1/2 by the MT peptide. In conclusion, the MT peptide could be detected in the respective target organs, therein mimicking the inhibitory *in vitro* effects of the MTMR7 FL enzyme on the RAS-ERK1/2 signaling cascade and tumour cell proliferation in two independent mouse models of GI cancer.

4. Discussion

Members of the MTM family are generally described as survival phosphatases promoting cellular proliferation and preventing apoptosis [53,54]. Opposing this paradigm, we previously provided evidence that MTMR7 concomitantly disrupts both ERK1/2 and PI3K signaling and increases the transcriptional activity of PPARγ, resulting in decreased proliferation of human cancer cells [14,15]. Here, we demonstrated a novel role for MTMR7 as a direct inhibitor of mutant RAS, which is the major upstream regulator of these signaling axes. Furthermore, we identified the CC domain of MTMR7 as the region responsible for signal inhibition. We show that the CC domain directly interacts with the globular domain (GD) of K-RAS preferably in its GDP-bound state. Using an MTMR7 CC-mimicking peptide (MT), we confirmed its anti-tumour efficacy in GI cancers *in vitro* and *in vivo*.

We localized the MTMR7 FL enzyme at endomembranes of endosomes and the ER, where it may lower the amount of PI(3)P and PI(3,5) P2. All RAS proteins require extensive posttranslational modifications for proper localization and signaling, and K-RAS binds to negatively charged membranes containing PS and PIPs at the endosomal compartment [4,10,45,55]. Our subcellular fractionation and IF experiments suggest a detachment of RAS from these (endo)membranes. Interestingly, we could not find evidence for an increase of soluble RAS (**S2**) indicating a rapid degradation of cytoplasmic RAS. MTMs shift the balance of poly-phosphorylated inositol moieties exposed at the inner leaflet of membrane bilayers in the vicinity of other negatively charged phospholipids like PS, to a less phosphorylated state [10,45]. However,
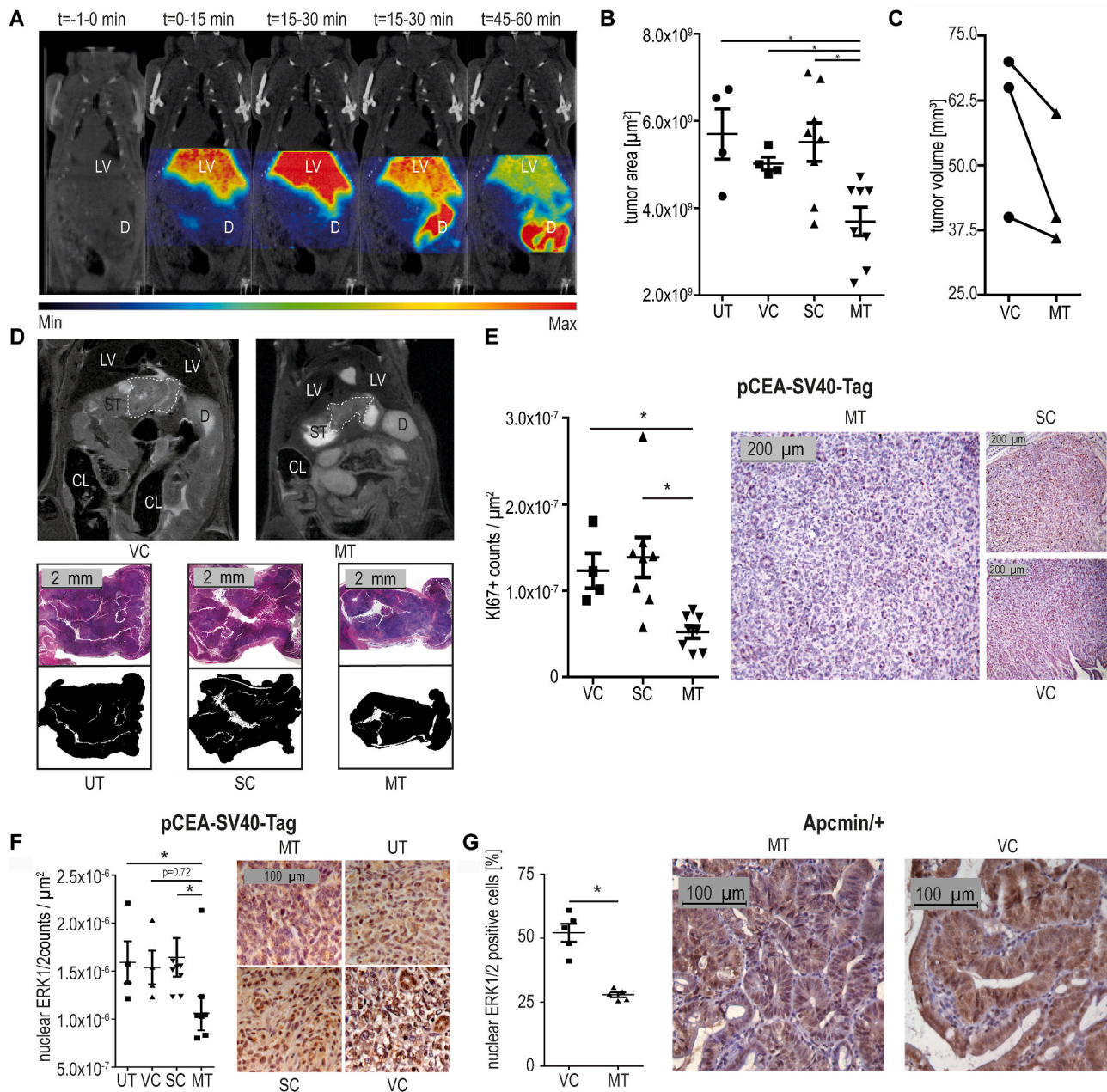
Fig. 7. MT peptide inhibits tumour growth *in vivo*. **A, Biodistribution of the MT peptide**. Representative averaged coronal PET images showing the abdominal region of a Wistar rat after tail-vein injection of 15.49 MBq of [^{18}F]MT under baseline conditions. PET images were averaged to four timeframes of 15 min each. LV: liver, D: duodenum. The colour bar indicates minimum and maximum uptake. **B, MT peptide reduces proliferation of murine gastric cancer *in vivo***. 2D quantification of tumour areas: *CEA424-SV4*0 TAg mice were left untreated (UT) or treated with vehicle control (VC), MT or SC peptides (i.p., 30 mg/kg per day, 4 times per week) for 2 weeks. H&E-stained FFPE tissue sections from stomachs were measured. Tumour areas were normalized to the area of the lamina muscularis mucosae and calculated as mean (μm^2) $\pm$ S.E. (*p $<$ 0.05 *vs.* MT, 1wayANOVA, Holm-Sidak's multiple comparisons test, n = 4–8 mice per group). **C, *In situ* detection of gastric tumours in mouse stomachs**. T1/T2 and diffusion weighted images from *CEA424-SV4*0 TAg mice treated with VC or MT peptide were analysed by MRI. Tumour volume in T2 weighted images was measured and calculated as mean (mm^3) (n = 3 mice per group). **D, Representative T2 weighted images (top) and H&E-stained FFPE tissue sections (bottom)**. The tumour is marked (circles with white or black dashed line; top). LV: liver, ST: stomach, D: duodenum, CL: colon. Black and white images representing the tumour areas used for planimetry are shown below the H&E sections. **E, Quantification of tumour cell proliferation**. FFPE tissue sections from *CEA424-SV4*0 TAg mice, treated as above, were subjected to IHC using Ki67 Ab. Ki67+ cells were counted in the tumour area of five fields per animal at a magnification of 100x. The number of Ki67+ cells was normalized to the tumour area in μm^2 visible in each field and calculated as mean $\pm$ S.E. (*p $<$ 0.05 *vs.* MT, 1wayANOVA, Holm-Sidak's multiple comparisons test, n = 4–8 mice per group). Original magnifications 100x, Scale bar = 200 μm. **F, Quantification of active ERK1/2 in *CEA424-SV4*0 TAg mice with gastric cancer**. In FFPE tissue sections from E, the number of ERK1/2+ nuclei (= cells with active ERK1/2 signaling) was counted in five fields per animal at a magnification of 100x normalized to the tumour area in μm^2 in the same field and calculated as mean $\pm$ S.E (*p $<$ 0.05 *vs.* MT, 1wayANOVA, Holm-Sidak's multiple comparisons test, n = 4–8 mice per group). Original magnifications 200x, Scale bar = 100 μm. **G, Quantification of active ERK1/2 in *Apc*$^{min/+}$ mice with intestinal cancer**. Mice were treated with VC or MT peptide (i.p., 30 mg/kg per day, 4 times per week) for 2 weeks. In FFPE tissue sections, numbers of ERK1/2+ nuclei were counted in five fields per animal at a magnification of 100x and presented as % $\pm$ S.E of all nuclei in tumour cells (*p $<$ 0.05 *vs.* MT, *t*-test, n = 5 mice per group). Original magnifications 200x, Scale bar = 100 μm.

depletion of the MTMR7 substrate PI(3)P did not alter MTMR7-mediated inhibition of RAS signaling, and MTMR7 overexpression did not alter the overall membrane potential (**S8**).

Thus, while MTMR7 and RAS proteins are localized at the same cellular compartments, the enzymatic activity of MTMR7 does not seem to be responsible for the inhibition of RAS signaling.

Since the CC domain-mimicking peptide achieved a very similar effect to the MTMR7 FL protein and lacks both the catalytic (HCS) site of the phosphatase and the N-terminal membrane-binding PH-GRAM domain, we suggest that inhibition of the RAS-ERK1/2-*FOS* axis is mediated by direct binding of the CC domain of MTMR7 to RAS, rather than by a direct impact on the cellular PIP pool, which constitutes only a very small fraction of total phospholipids in eukaryotic cells [10]. Our NMR studies gave a first picture of where and how MTMR7 interacts with K-RAS4B. The interaction occurs with the GD mainly through a mixture of hydrophobic and electrostatic interactions, including, most notably, three out of the four positive charges within the CC sequence of MTMR7. This also makes it unlikely that it would be an oligomeric state of M7-CC that could bind RAS, as these residues were found to be necessary for CC formation (Fig. 5) making them unavailable for dimer formation. It was possible to facilitate the interaction by detaching or removing the HVR. The interaction remains to be extensively characterized, but it seems plausible that the binding of the CC domain might efficiently stabilize the inactive GDP-bound state of K-RAS, as we saw much weaker binding to GTP-loaded K-RAS, and overexpression of

MTMR7 FL enzyme led to a decrease of active, i.e., GTP-loaded RAS (Fig. 5A). The effect of the nucleotide-cargo on M7-CC binding that we observed in the WT, was more pronounced for K-RAS^{G12V}. M7-CC bound only very weakly to the GTP-bound state of K-RAS4B^{G12V}, making the nucleotide dependency of the binding stronger for the cancer mutant than for the WT (Fig. 5C). Also, M7-CC binding to GDP-bound KRAS^{G12V} was weaker than to GDP-bound K-RAS^{WT}.

Conformational dynamics describing sampling of an active-like state of GDP-bound K-RAS^{G12V} have already been investigated computationally, incorporating NMR and crystallography data [56]. This is supported by our data, where M7-CC greatly favours binding to the GDP-bound and likely inactive K-RAS^{WT} with weaker binding to GDP-bound K-RAS^{G12V}, a variant which samples the active state more readily. We hypothesize that this sampling of both active and inactive states is a universal trait of K-RAS GDs, and that nucleotide binding merely shifts the likelihood of finding K-RAS4B in one or the other state (GDP for inactive, GTP for active). M7-CC may bind the GD only when it visits the inactive state and enable trapping of K-RAS in this state. This conclusion is supported by the observation that M7-CC binds to the GTP-bound K-RAS, but weaker than to the GDP-bound K-RAS. A similar preference for the GDP-state was observed for covalent inhibitors of K-RAS^{G12C}. The inhibitor ARS-853 conjugates rapidly to C12 immediately after GTP-hydrolysis, preventing the exchange of the newly formed GDP with GTP [57]. Whether M7-CC just stabilizes the inactive state or also prevents nucleotide exchange, like ARS-853, needs to be further investigated.
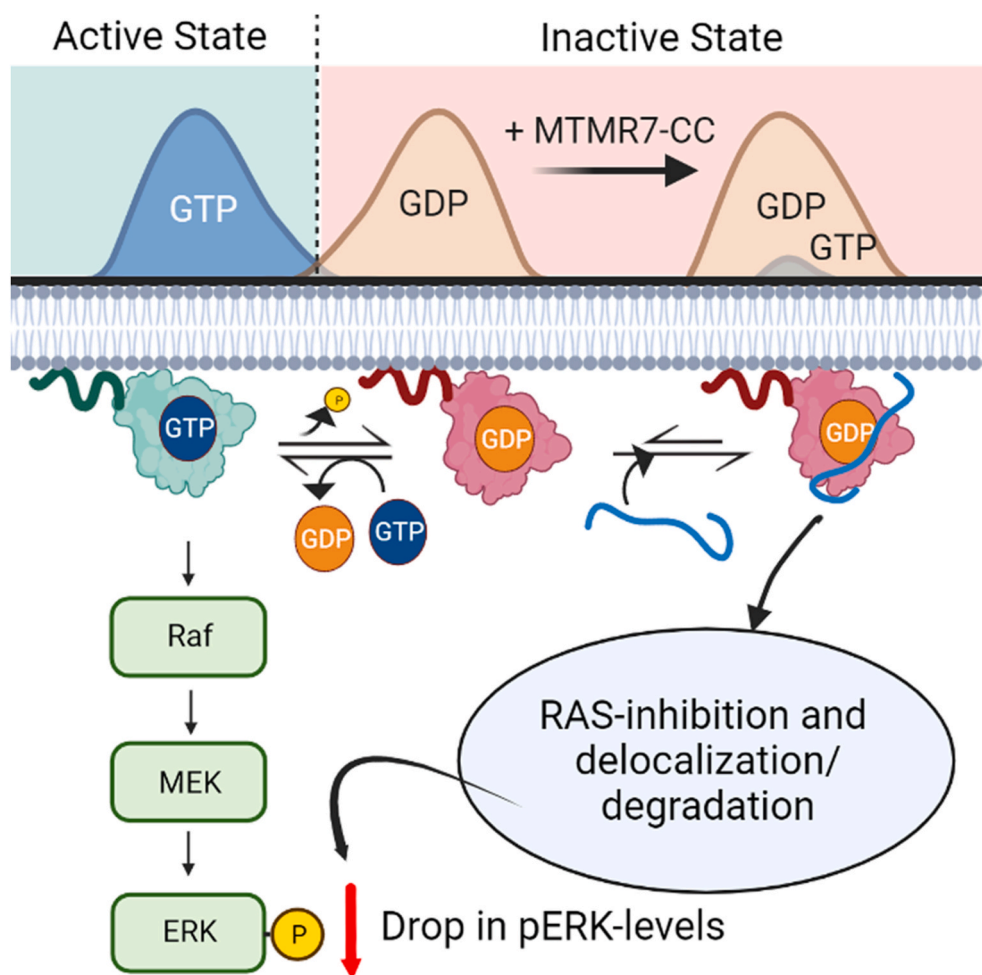

Fig. 8. MTMR7 binds directly to specific K-RAS states. MTMR7-CC prefers binding to GDP-bound K-RAS over GTP-bound K-RAS. GDP-bound K-RAS populates the inactive state, which would be stabilized by MTMR7-CC (upper panel). Within the cell (lower panel), this preference might translate to MTMR7-CC binding to GDP-bound RAS, leading to depletion of the active state from the RAS equilibrium, thereby lowering overall RAS levels over time. This illustration was generated using biorender.com.

The fact that we needed to detach the HVR from the GD by increasing the salt concentration or by removing it to observe an interaction with the K-RAS protein, may be a hint towards the M7-CC binding site: It strongly suggest that the CC domain of MTMR7 competes with the positively charged tail of K-RAS4B for the same binding sites on the GD, which may be more accessible in the inactive state. It has been shown that the HVR of K-RAS can interact with the GD of K-RAS through electrostatic interactions and does so with especially high affinity when K-RAS is in the GDP-bound, inactive state [24].

In conclusion, MTMR7 may inhibit (K)-RAS via interaction between its CC domain and the globular domain (GD) of RAS, stabilizing an inactive GDP-bound state, an effect accompanied by a reduction in membrane-bound RAS and a possible increase in its degradation [55] (Fig. 8). Consequently, lowered RAS activity and/or stability culminates in inhibition of proliferation of *KRAS*-mutated cancer cells, thus making K-RAS directly druggable for novel treatment interventions. Future studies are needed to fully elucidate the details of this mechanism and discern its relevance for the three human *RAS* genes (*K/N/HRAS*) and the K-RAS protein variants (KRAS4A/B), which make unique contributions to tumour formation in given organs and tissues.

In its role as a potential future therapeutic, we also characterized the MT peptide. Biophysical studies on this synthetic peptide and the extended recombinant M7-CC domain showed that both are disordered at low concentrations with increasing folding at higher concentrations, stabilized in a two-step process. These results may contribute to a better understanding of the structural behaviour of the CC domain of MTMs in general. While homodimerization was so far not been shown for MTMR7 [58], the oligomer appears dynamic as it cannot be directly observed by NMR and only forms at high concentrations. At cellular concentrations, homodimerization might be negligible in the cytosol, also considering the presence of MTMR9 as a competing heterodimerization partner. For the peptide as a potential drug, concentration-dependent structural changes could be either detrimental or favourable. For other lipidated therapeutic peptides, the oligomeric state affected protein binding affinity [59], and it will be important to decipher which stoichiometry is most beneficial therapeutically and how to stabilize this state further.

The NMR results provide a starting point for this, identifying stretches within the M7-CC with higher helical propensity than others. Such trigger-sequence feature is common in CCs and is indispensable for folding [60], forming inter- and intramolecular salt bridges to stabilize the structure [61,62]. The longest of the helical stretches in M7-CC, also present in the MT peptide, covers the dominantly positively charged region shown to interact with K-RAS. Trigger sequences are of interest for CC optimization, since introducing or stabilizing them can increase stability [63]. Designing variants of the MT peptide with altered stability of the trigger sequence or covalently linked in dimers or tetramers, and subsequently investigating their effect on GI cancer cell growth, could be an important next step that could pave the way towards more specific and reliable peptide-based drugs for cancer therapy.

A question remains as to whether the MT peptide can fully substitute for the MTMR7 FL enzyme regarding anti-tumoral efficacies *in vitro* and *in vivo*. We did observe lack of PI3K/AKT-inhibition by the peptide as opposed to the FL enzyme. Thus, the full tumour suppressor potential may result from a combination of the enzymatic and heterodimerization effects of MTMR7, e.g. by binding to CC partners like MTMR9 [12], PPARγ [14,15] or K-RAS. Future mutagenesis studies will be required to fine-map the interactome of MTMR7. Squelching of signaling hubs by adaptor or scaffolding molecules, as exemplified here by the leucine zipper-like CC domains of MTMR7, may be superior to direct covalent inhibition of RAS to prevent drug-induced resistance over prolonged treatment times, a major obstacle for almost all small molecule-based treatments, which have been found to favour selection of drug-resistant clones in tumours. However, the either unknown or complex pharmacodynamics and -kinetics of peptides and peptidomimetics (e.g., nutlins, exenatide) is a serious draw-back and a cause of failure and high attrition rates during pre/clinical development phases.

In summary, we have shown that MTMR7 functions as a tumour suppressor, which, by directly targeting mutant K-RAS via its CC domain downstream of the EGFR, inhibits proliferation and survival pathways in *KRAS*-mutated cancer cells elicited by RAS effectors. Mimicking MTMR7 may thus be a promising approach for treatment of *KRAS*-mutated tumours as opposed to the currently used BRAF, MEK1/2 [64] or mTOR inhibitors, which by targeting single signaling tiers lead to compensatory up-regulation, shunting and defective negative feed-back loops culminating in failure of clinical responses in patients [65,66]. Based on our previous evidence [15] that loss of MTMR7 is a frequent event in e. g., colorectal cancer, pharmacological replenishment of this tumour suppressor network by exogenous administration of cell-permeable MTMR7-CC mimicry peptide(s) [14,15] or future peptidomimetics may provide a rationale for destroying mutant RAS and re-sensitize *RAS*-mutated tumour cells to clinical therapies targeting the EGFR (e. g., cetuximab) [1,3], regimens otherwise limited to a small subgroup of RAS WT patients.

Data availability

NMR chemical shift data were deposited in the Biological Magnetic Resonance Data Bank BMRB (https://bmrb.io/) under the accession ID 52269.

CRediT authorship contribution statement

Philip Weidner: Writing – review & editing, Writing – original draft, Visualization, Validation, Methodology, Investigation, Funding acquisition, Formal analysis, Data curation, Conceptualization. **Daniel Saar:** Writing – review & editing, Writing – original draft, Visualization, Validation, Software, Resources, Methodology, Investigation, Funding acquisition, Formal analysis, Data curation, Conceptualization. **Michaela Söhn:** Visualization, Methodology, Investigation, Formal analysis, Data curation. **Torsten Schroeder:** Visualization, Methodology, Investigation, Formal analysis, Data curation. **Yanxiong Yu:** Visualization, Methodology, Investigation, Data curation. **Frank G. Zöllner:** Visualization, Software, Resources, Methodology, Investigation, Formal analysis, Data curation. **Norbert Ponelies:** Methodology, Investigation. **Xiaobo Zhou:** Visualization, Validation, Software, Resources, Methodology, Investigation, Formal analysis, Data curation. **André Zwicky:** Visualization, Validation, Software, Resources, Methodology, Investigation, Formal analysis, Data curation. **Florian N. Rohrbacher:** Resources, Methodology, Investigation. **Vijaya R. Pattabiraman:** Visualization, Validation, Software, Resources, Methodology,

Investigation, Formal analysis, Data curation. **Matthias Tanriver:** Visualization, Validation, Software, Resources, Methodology, Investigation, Formal analysis, Data curation. **Alexander Bauer:** Resources, Methodology, Investigation. **Hazem Ahmed:** Visualization, Validation, Software, Resources, Methodology, Investigation, Formal analysis, Data curation. **Simon M. Ametamey:** Visualization, Validation, Software, Resources, Methodology, Investigation, Formal analysis, Data curation. **Philipp Riffel:** Validation, Software, Methodology, Investigation, Formal analysis. **Rony Seger:** Writing – review & editing, Supervision, Funding acquisition, Conceptualization. **Jeffrey W. Bode:** Writing – original draft, Visualization, Validation, Supervision, Software, Resources, Methodology, Investigation, Formal analysis, Data curation. **Rebecca C. Wade:** Writing – review & editing, Supervision, Software, Resources, Methodology, Investigation, Conceptualization. **Matthias P. A. Ebert:** Writing – review & editing, Supervision, Resources, Project administration, Funding acquisition. **Birthe B. Kragelund:** Writing – review & editing, Writing – original draft, Visualization, Validation, Supervision, Software, Resources, Project administration, Methodology, Investigation, Funding acquisition, Formal analysis, Data curation, Conceptualization. **Elke Burgermeister:** Writing – review & editing, Writing – original draft, Visualization, Validation, Supervision, Resources, Project administration, Methodology, Investigation, Funding acquisition, Formal analysis, Data curation, Conceptualization.

Declaration of competing interest

The authors declare that they have no known competing financial interests or personal relationships that could have appeared to influence the work reported in this paper.

Appendix A. Supplementary data

Supplementary data to this article can be found online at https://doi.org/10.1016/j.canlet.2024.216783.

References

[1] N. Tebbutt, M.W. Pedersen, T.G. Johns, Targeting the ERBB family in cancer: couples therapy, Nat. Rev. Cancer 13 (2013) 663–673.

[2] C.G.A. Network, Comprehensive molecular characterization of human colon and rectal cancer, Nature 487 (2012) 330–337.

[3] C.S. Karapetis, S. Khambata-Ford, D.J. Jonker, C.J. O'Callaghan, D. Tu, N. C. Tebbutt, R.J. Simes, H. Chalchal, J.D. Shapiro, S. Robitaille, T.J. Price, L. Shepherd, H.J. Au, C. Langer, M.J. Moore, J.R. Zalcberg, K-ras mutations and benefit from cetuximab in advanced colorectal cancer, N. Engl. J. Med. 359 (2008) 1757–1765.

[4] A.D. Cox, S.W. Fesik, A.C. Kimmelman, J. Luo, C.J. Der, Drugging the undruggable RAS: mission possible? Nat. Rev. Drug Discov. 13 (2014) 828–851.

[5] G. Maik-Rachline, R. Seger, The ERK cascade inhibitors: towards overcoming resistance, Drug Resist. Updates 25 (2016) 1–12.

[6] F. Skoulidis, B.T. Li, G.K. Dy, T.J. Price, G.S. Falchook, J. Wolf, A. Italiano, M. Schuler, H. Borghaei, F. Barlesi, T. Kato, A. Curioni-Fontecedro, A. Sacher, A. Spira, S.S. Ramalingam, T. Takahashi, B. Besse, A. Anderson, A. Ang, Q. Tran, O. Mather, H. Henary, G. Ngarmchamnanrith, G. Friberg, V. Velcheti, R. Govindan, Sotorasib for lung cancers with KRAS p.G12C mutation, N. Engl. J. Med. 384 (2021) 2371–2381.

[7] A. Plangger, B. Rath, S. Stickler, M. Hochmair, C. Lang, L. Weigl, M. Funovics, G. Hamilton, Cytotoxicity of combinations of the pan-KRAS SOS1 inhibitor BAY-293 against pancreatic cancer cell lines, Discov Oncol 13 (2022) 84.

[8] S. Lu, H. Jang, J. Zhang, R. Nussinov, Inhibitors of ras-SOS interactions, ChemMedChem 11 (2016) 814–821.

[9] Y. Zhou, C.O. Wong, K.J. Cho, D. van der Hoeven, H. Liang, D.P. Thakur, J. Luo, M. Babic, K.E. Zinsmaier, M.X. Zhu, H. Hu, K. Venkatachalam, J.F. Hancock, SIGNAL TRANSDUCTION. Membrane potential modulates plasma membrane phospholipid dynamics and K-Ras signaling, Science 349 (2015) 873–876.

[10] J.F. Hancock, Ras proteins: different signals from different locations, Nat. Rev. Mol. Cell Biol. 4 (2003) 373–384.

[11] K. Iwabuchi, K. Handa, S. Hakomori, Separation of "glycosphingolipid signaling domain" from caveolin-containing membrane fraction in mouse melanoma B16 cells and its role in cell adhesion coupled with signaling, J. Biol. Chem. 273 (1998) 33766–33773.

[12] Y. Mochizuki, P.W. Majerus, Characterization of myotubularin-related protein 7 and its binding partner, myotubularin-related protein 9, Proc. Natl. Acad. Sci. U. S. A. 100 (2003) 9768–9773.

[13] A.S. Nicot, J. Laporte, Endosomal phosphoinositides and human diseases, Traffic 9 (2008) 1240–1249.

[14] P. Weidner, M. Sohn, T. Schroeder, L. Helm, V. Hauber, T. Gutting, J. Betge, C. Rocken, F.N. Rohrbacher, V.R. Pattabiraman, J.W. Bode, R. Seger, D. Saar, A. Nunes-Alves, R.C. Wade, M.P.A. Ebert, E. Burgermeister, Myotubularin-related protein 7 activates peroxisome proliferator-activated receptor-gamma, Oncogenesis 9 (2020) 59.

[15] P. Weidner, M. Sohn, T. Gutting, T. Friedrich, T. Gaiser, J. Magdeburg, P. Kienle, H. Ruh, C. Hopf, H.M. Behrens, C. Rocken, T. Hanoch, R. Seger, M.P. Ebert, E. Burgermeister, Myotubularin-related protein 7 inhibits insulin signaling in colorectal cancer, Oncotarget 7 (2016) 50490–50506.

[16] K. Hnia, I. Vaccari, A. Bolino, J. Laporte, Myotubularin phosphoinositide phosphatases: cellular functions and disease pathophysiology, Trends Mol. Med. 18 (2012) 317–327.

[17] J. Zou, C. Zhang, J. Marjanovic, M.V. Kisseleva, P.W. Majerus, M.P. Wilson, Myotubularin-related protein (MTMR) 9 determines the enzymatic activity, substrate specificity, and role in autophagy of MTMR8, Proc. Natl. Acad. Sci. U. S. A. 109 (2012) 9539–9544.

[18] T. Balla, M. Wymann, J.D. York, Phosphoinositides I Enzymes of Synthesis and Degradation, Subcellular Biochemistry, Springer, Dordrecht ; New York, 2012, p. 1, online resource (xv, 352 p.).

[19] C. Cao, J.M. Backer, J. Laporte, E.J. Bedrick, A. Wandinger-Ness, Sequential actions of myotubularin lipid phosphatases regulate endosomal PI(3)P and growth factor receptor trafficking, Mol. Biol. Cell 19 (2008) 3334–3346.

[20] E. Burgermeister, A. Schnoebelen, A. Flament, J. Benz, M. Stihle, B. Gsell, A. Rufer, A. Ruf, B. Kuhn, H.P. Marki, J. Mizrahi, E. Sebokova, E. Niesor, M. Meyer, A novel partial agonist of peroxisome proliferator-activated receptor-gamma (PPARgamma) recruits PPARgamma-coactivator-1alpha, prevents triglyceride accumulation, and potentiates insulin signaling in vitro, Mol. Endocrinol. 20 (2006) 809–830.

[21] Y. Zhang, T. Hirota, K. Kuwata, S. Oishi, S.G. Gramani, J.W. Bode, Chemical synthesis of atomically tailored SUMO E2 conjugating enzymes for the formation of covalently linked SUMO-E2-E3 ligase ternary complexes, J. Am. Chem. Soc. 141 (2019) 14742–14751.

[22] D. Reverter, C.D. Lima, Preparation of SUMO proteases and kinetic analysis using endogenous substrates, Methods Mol. Biol. 497 (2009) 225–239.

[23] F.W. Studier, Protein production by auto-induction in high density shaking cultures, Protein Expr. Purif. 41 (2005) 207–234.

[24] T.S. Chavan, H. Jang, L. Khavrutskii, S.J. Abraham, A. Banerjee, B.C. Freed, L. Johannessen, S.G. Tarasov, V. Gaponenko, R. Nussinov, N.I. Tarasova, High-affinity interaction of the K-Ras4B hypervariable region with the ras active site, Biophys. J. 109 (2015) 2602–2613.

[25] J. Thompson, T. Epting, G. Schwarzkopf, A. Singhofen, A.M. Eades-Perner, H. van Der Putten, W. Zimmermann, A transgenic mouse line that develops early-onset invasive gastric carcinoma provides a model for carcinoembryonic antigen-targeted tumor therapy, Int. J. Cancer 86 (2000) 863–869.

[26] F. Lian, X. Xing, G. Yuan, C. Schafer, S. Rauser, A. Walch, C. Rocken, M. Ebeling, M. B. Wright, R.M. Schmid, M.P. Ebert, E. Burgermeister, Farnesoid X receptor protects human and murine gastric epithelial cells against inflammation-induced damage, Biochem. J. 438 (2011) 315–323.

[27] E. Burgermeister, D. Chuderland, T. Hanoch, M. Meyer, M. Liscovitch, R. Seger, Interaction with MEK causes nuclear export and downregulation of peroxisome proliferator-activated receptor gamma, Mol. Cell Biol. 27 (2007) 803–817.

[28] M.P. Ebert, M. Tanzer, B. Balluff, E. Burgermeister, A.K. Kretzschmar, D.J. Hughes, R. Tetzner, C. Lofton-Day, R. Rosenberg, A.C. Reinacher-Schick, K. Schulmann, A. Tannapfel, R. Hofheinz, C. Rocken, G. Keller, R. Langer, K. Specht, R. Porschen, J. Stohlmacher-Williams, T. Schuster, P. Strobel, R.M. Schmid, TFAP2E-DKK4 and chemoresistance in colorectal cancer, N. Engl. J. Med. 366 (2012) 44–53.

[29] E. Burgermeister, R. Seger, MAPK kinases as nucleo-cytoplasmic shuttles for PPARgamma, Cell Cycle 6 (2007) 1539–1548.

[30] B. Forood, E.J. Feliciano, K.P. Nambiar, Stabilization of alpha-helical structures in short peptides via end capping, Proc. Natl. Acad. Sci. U. S. A. 90 (1993) 838–842.

[31] V. Munoz, L. Serrano, Elucidating the folding problem of helical peptides using empirical parameters. III. Temperature and pH dependence, J. Mol. Biol. 245 (1995) 297–308.

[32] V. Munoz, L. Serrano, Elucidating the folding problem of helical peptides using empirical parameters. II. Helix macrodipole effects and rational modification of the helical content of natural peptides, J. Mol. Biol. 245 (1995) 275–296.

[33] V. Munoz, L. Serrano, Elucidating the folding problem of helical peptides using empirical parameters, Nat. Struct. Biol. 1 (1994) 399–409.

[34] F. Delaglio, S. Grzesiek, G.W. Vuister, G. Zhu, J. Pfeifer, A. Bax, NMRPipe: a multidimensional spectral processing system based on UNIX pipes, J. Biomol. NMR 6 (1995) 277–293.

[35] W.F. Vranken, W. Boucher, T.J. Stevens, R.H. Fogh, A. Pajon, M. Llinas, E.L. Ulrich, J.L. Markley, J. Ionides, E.D. Laue, The CCPN data model for NMR spectroscopy: development of a software pipeline, Proteins 59 (2005) 687–696.

[36] V.Y. Orekhov, V.A. Jaravine, Analysis of non-uniformly sampled spectra with multi-dimensional decomposition, Prog. Nucl. Magn. Reson. Spectrosc. 59 (2011) 271–292.

[37] J.T. Nielsen, F.A.A. Mulder, POTENCI: prediction of temperature, neighbor and pH-corrected chemical shifts for intrinsically disordered proteins, J. Biomol. NMR 70 (2018) 141–165.

[38] C.W. Wood, D.N. Woolfson, CCBuilder 2.0: powerful and accessible coiled-coil modeling, Protein Sci. 27 (2018) 103–111.

[39] E. Krieger, G. Koraimann, G. Vriend, Increasing the precision of comparative models with YASARA NOVA–a self-parameterizing force field, Proteins 47 (2002) 393–402.

[40] A. Chiotellis, H. Ahmed, T. Betzel, M. Tanriver, C.J. White, H. Song, S. Da Ros, R. Schibli, J.W. Bode, S.M. Ametamey, Chemoselective (18)F-incorporation into pyridyl acyltrifluoroborates for rapid radiolabelling of peptides and proteins at room temperature, Chem. Commun. 56 (2020) 723–726.

[41] S.D. Kramer, T. Betzel, L. Mu, A. Haider, A.M. Herde, A.K. Boninsegni, C. Keller, M. Szermerski, R. Schibli, B. Wunsch, S.M. Ametamey, Evaluation of (11)C-Me-NB1 as a potential PET radioligand for measuring GluN2B-containing NMDA receptors, drug occupancy, and receptor cross talk, J. Nucl. Med. 59 (2018) 698–703.

[42] M.W. Pfaffl, A new mathematical model for relative quantification in real-time RT–PCR, Nucleic Acids Res. 29 (2001) e45-e45.

[43] E. Cerami, J. Gao, U. Dogrusoz, B.E. Gross, S.O. Sumer, B.A. Aksoy, A. Jacobsen, C. J. Byrne, M.L. Heuer, E. Larsson, Y. Antipin, B. Reva, A.P. Goldberg, C. Sander, N. Schultz, The cBio cancer genomics portal: an open platform for exploring multidimensional cancer genomics data, Cancer Discov. 2 (2012) 401–404.

[44] S. Bolte, F.P. Cordelieres, A guided tour into subcellular colocalization analysis in light microscopy, J. Microsc. 224 (2006) 213–232.

[45] M. Gelabert-Baldrich, D. Soriano-Castell, M. Calvo, A. Lu, A. Vina-Vilaseca, C. Rentero, A. Pol, S. Grinstein, C. Enrich, F. Tebar, Dynamics of KRas on endosomes: involvement of acidic phospholipids in its association, Faseb. J. 28 (2014) 3023–3037.

[46] J. Barretina, G. Caponigro, N. Stransky, K. Venkatesan, A.A. Margolin, S. Kim, C. J. Wilson, J. Lehar, G.V. Kryukov, D. Sonkin, A. Reddy, M. Liu, L. Murray, M. F. Berger, J.E. Monahan, P. Morais, J. Meltzer, A. Korejwa, J. Jane-Valbuena, F. A. Mapa, J. Thibault, E. Bric-Furlong, P. Raman, A. Shipway, I.H. Engels, J. Cheng, G.K. Yu, J. Yu, P. Aspesi Jr., M. de Silva, K. Jagtap, M.D. Jones, L. Wang, C. Hatton, E. Palescandolo, S. Gupta, S. Mahan, C. Sougnez, R.C. Onofrio, T. Liefeld, L. MacConaill, W. Winckler, M. Reich, N. Li, J.P. Mesirov, S.B. Gabriel, G. Getz, K. Ardlie, V. Chan, V.E. Myer, B.L. Weber, J. Porter, M. Warmuth, P. Finan, J. L. Harris, M. Meyerson, T.R. Golub, M.P. Morrissey, W.R. Sellers, R. Schlegel, L. A. Garraway, The Cancer Cell Line Encyclopedia enables predictive modelling of anticancer drug sensitivity, Nature 483 (2012) 603–607.

[47] T. Friedrich, M. Sohn, T. Gutting, K.P. Janssen, H.M. Behrens, C. Rocken, M.P. A. Ebert, E. Burgermeister, Subcellular compartmentalization of docking protein-1 contributes to progression in colorectal cancer, EBioMedicine 8 (2016) 159–172.

[48] B. Wasylyk, J. Hagman, A. Gutierrez-Hartmann, Ets transcription factors: nuclear effectors of the Ras-MAP-kinase signaling pathway, Trends Biochem. Sci. 23 (1998) 213–216.

[49] P.S. Millard, K. Bugge, R. Marabini, W. Boomsma, M. Burow, B.B. Kragelund, IDDomainSpotter: compositional bias reveals domains in long disordered protein regions-Insights from transcription factors, Protein Sci. 29 (2020) 169–183.

[50] M.A. Raess, S. Friant, B.S. Cowling, J. Laporte, Wanted - dead or alive: myotubularins, a large disease-associated protein family, Adv Biol Regul 63 (2017) 49–58.

[51] J.N. Kather, A. Weidner, U. Attenberger, Y. Bukschat, C.A. Weis, M. Weis, L. R. Schad, F.G. Zollner, Color-coded visualization of magnetic resonance imaging multiparametric maps, Sci. Rep. 7 (2017) 41107.

[52] D.A. Berti, R. Seger, The nuclear translocation of ERK, Methods Mol. Biol. 1487 (2017) 175–194.

[53] J.P. MacKeigan, L.O. Murphy, J. Blenis, Sensitized RNAi screen of human kinases and phosphatases identifies new regulators of apoptosis and chemoresistance, Nat. Cell Biol. 7 (2005) 591–600.

[54] J. Zou, S.C. Chang, J. Marjanovic, P.W. Majerus, MTMR9 increases MTMR6 enzyme activity, stability, and role in apoptosis, J. Biol. Chem. 284 (2008) 2064–2071.

[55] A. Lu, F. Tebar, B. Alvarez-Moya, C. Lopez-Alcala, M. Calvo, C. Enrich, N. Agell, T. Nakamura, M. Matsuda, O. Bachs, A clathrin-dependent pathway leads to KRas signaling on late endosomes en route to lysosomes, J. Cell Biol. 184 (2009) 863–879.

[56] P. Grudzien, H. Jang, N. Leschinsky, R. Nussinov, V. Gaponenko, Conformational dynamics allows sampling of an "Active-like" state by oncogenic K-Ras-GDP, J. Mol. Biol. 434 (2022) 167695.

[57] Q. Zhao, R. Haga, S. Tamura, I. Shimada, N. Nishida, Real-time monitoring of the reaction of KRAS G12C mutant specific covalent inhibitor by in vitro and in-cell NMR spectroscopy, Sci. Rep. 13 (2023) 19253.

[58] Y. Mochizuki, P.W. Majerus, Characterization of myotubularin-related protein 7 and its binding partner, myotubularin-related protein 9, Proc. Natl. Acad. Sci. USA 100 (2003) 9768–9773.

[59] M. Gallo, D. Vanni, S. Esposito, N. Alaimo, F. Orvieto, F. Rulli, A. Missineo, F. Caretti, F. Bonelli, M. Veneziano, L. Orsatti, E. Monteagudo, Oligomerization, albumin binding and catabolism of therapeutic peptides in the subcutaneous compartment: an investigation on lipidated GLP-1 analogs, J. Pharm. Biomed. Anal. 210 (2022) 114566.

[60] M.O. Steinmetz, I. Jelesarov, W.M. Matousek, S. Honnappa, W. Jahnke, J. H. Missimer, S. Frank, A.T. Alexandrescu, R.A. Kammerer, Molecular basis of coiled-coil formation, Proc. Natl. Acad. Sci. U. S. A. 104 (2007) 7062–7067.

[61] P. Burkhard, R.A. Kammerer, M.O. Steinmetz, G.P. Bourenkov, U. Aebi, The coiled-coil trigger site of the rod domain of cortexillin I unveils a distinct network of interhelical and intrahelical salt bridges, Structure 8 (2000) 223–230.

[62] P. Burkhard, J. Stetefeld, S.V. Strelkov, Coiled coils: a highly versatile protein folding motif, Trends Cell Biol. 11 (2001) 82–88.

[63] I. Drobnak, H. Gradisar, A. Ljubetic, E. Merljak, R. Jerala, Modulation of coiled-coil dimer stability through surface residues while preserving pairing specificity, J. Am. Chem. Soc. 139 (2017) 8229–8236.

[64] T. Zhan, G. Ambrosi, A.M. Wandmacher, B. Rauscher, J. Betge, N. Rindtorff, R. S. Haussler, I. Hinsenkamp, L. Bamberg, B. Hessling, K. Muller-Decker, G. Erdmann, E. Burgermeister, M.P. Ebert, M. Boutros, MEK inhibitors activate Wnt signalling and induce stem cell plasticity in colorectal cancer, Nat. Commun. 10 (2019) 2197.

[65] P. Lito, N. Rosen, D.B. Solit, Tumor adaptation and resistance to RAF inhibitors, Nat. Med. 19 (2013) 1401–1409.

[66] F. Chiarini, C. Evangelisti, J.A. McCubrey, A.M. Martelli, Current treatment strategies for inhibiting mTOR in cancer, Trends Pharmacol. Sci. 36 (2015) 124–135.